	الجـــمــهوريـــــة الـجــــزائريــــة الـديمقـــراطيـــة الـشعبيــــة	
	People's Democratic Republic of Algeria	
	وزارة الـتـعـلـيـــــم الــعـالــي والـبحـث الـعلـــمـي	
	Ministry of Higher Education and Scientific Research	
	جـــــامـعــــــة عبد الحميـــد بن باديـــس ـمستغانــــم	
	Abdel Hamid Ibn Badis University – Mostaganem	
	كليـــــــة الـعلــــوم والــتكنولـــوجـــــيـــا	
	Faculty of Sciences and Technology	
	قــسم الهنــــدســـة الميكانيكية	
	Department of Mechanical Engineering	

Registration number N°: M....../GM/2026

END-OF-STUDIES THESIS ACADEMIC MASTER'S DEGREE

Field: Mechanical Engineering
Specialization: Energy

Numerical analysis of the effect of fins on heat transfer in a rotary kiln

Presented by:
1-HAIRECH Laid
2-BETTICHE Faycel

Defended on 29/06/2026 before the jury composed:

President:	GUERMAT ABDELKADER	Associate Professor	University of Mostaganem UMAB
Examiner:	FLITTI ABDELMADJID	Associate Professor	University of Mostaganem UMAB
Supervisor:	ATTOU Youcef	Associate Professor	University of Mostaganem UMAB

Academic year: 2025 / 2026

Dedication

First and foremost, we thank Allah, the Almighty, for granting us the health, strength, and patience necessary to accomplish this work.

We would like to express our gratitude to our parents alive or dead, and ask Allah to put mercy on their souls. We would have loved if they were here to witness our efforts and success.

We would also like to extend our sincere thanks to our families for their presence, encouragement, and confidence throughout this journey.

Thanking

Praise be to God, who granted us patience in times of need, strength in moments of weakness, and determination in the face of despair.

We would like to express our sincere gratitude to our supervisor, Dr. Attou Youcef, for his kindness, valuable advice, and continuous guidance throughout every stage of this work.

We also wish to extend our heartfelt thanks to the president Dr Guermat Abdelkader and the member of the jury Dr Flitti Abdelmadjid for the honor they have bestowed upon us by evaluating and examining this work.

We would like to thank all our friends and colleagues, as well as everyone who encouraged and supported us, directly or indirectly, during the completion of this work.

THANK YOU ALL!

LIST OF FIGURES

LIST OF TABLES

Nomenclature

SYMBOL	DESCRIPTION	UNIT
L	Length of the kiln	[m]
D	Kiln diameter	[m]
d	Burner diameter	[m]
T	Temperature	[K]
d_h	Hydraulic diameter	[m]
V	axial speed of fluid	[m.s-1]
Nu	Nusselt number	/
Cf	friction of Coefficient	/
k	Turbulence kinetic energy	[m2.s-2]
h	Convective heat transfer coefficient	[W.m-2.K-1]

Greek symbols

SYMBOL	DESCRIPTION	UNIT
ρ	Fluid density	[kg/m3]
λ	Thermal conductivity	[W.m-1. K-1]
v	Kinematic viscosity	[m2.s-1]
ε	Turbulence dissipation rate	[m2.s-3]
vt	Turbulent kinematic viscosity	[m2.s-1]
ω	Specific dissipation rate	[s-1]

الملخص

تقدم هذه الأطروحة دراسة عددية تعتمد على ديناميكا الموائع الحسابية (CFD) بهدف تحليل تأثير الزعانف المولدة للاضطراب من نوع Shark-fin على تحسين انتقال الحرارة داخل الفرن الدوار. ويتمثل الهدف الرئيسي في تحديد التكوين الهندسي الأمثل الذي يسمح بتحسين الأداء الحراري مع تقليل الفواقد الديناميكية المصاحبة.
تم تطوير نموذج عددي ثنائي الأبعاد باستخدام نموذج الاضطراب **SST k-ω** لدراسة الظواهر الحرارية والهيد وديناميكية. وقد تم تحليل عدة معايير، منها: توزيع درجة الحرارة، عدد نوسلت الموضعي، معامل الاحتكاك، الطاقة الحركية الاضطرابية(TKE) ، وخطوط الجريان.
شملت الدراسة البارامترية ثلاث متغيرات هندسية رئيسية:

- عدد الزعانف.
- عمق الزعانف.
- زاوية ميل الزعانف.

أظهرت النتائج أن إضافة الزعانف تؤدي إلى تحسين انتقال الحرارة مقارنة بالحالة المرجعية دون زعانف، وذلك بفضل تكوين مناطق إعادة تدوير الجريان وتحسين عملية الخلط بين المائع القريب من الجدار والمائع الموجود في مركز المجرى. ومع ذلك، فإن الزيادة المفرطة في عدد الزعانف أو عمقها أو زاوية ميلها تؤدي إلى ارتفاع ملحوظ في فقدان الضغط ومعامل الاحتكاك.
وبعد مقارنة مختلف التكوينات المدروسة، تبيّن أن أفضل أداء حراري–هيدروليكي إجمالي تم الحصول عليه عند التكوين التالي:
5زعانف – عمق الزعنفة – Dp = 0.5 زاوية الميل.$\alpha = 30°$
الكلمات المفتاحية:
عدد الزعانف، انتقال الحرارة، معامل الاحتكاك، رقم نوسلت، الطاقة الحركية للاضطراب.

Résumé

Ce travail de mémoire porte sur une étude numérique basée sur la méthode CFD afin d'analyser l'influence des ailettes turbulence de type Shark-fin sur l'amélioration du transfert thermique dans un four rotatif. L'objectif principal est de déterminer une configuration géométrique optimale permettant d'améliorer les performances thermiques tout en réduisant les pertes dynamique associées Un modèle numérique bidimensionnel a été développé en utilisant le modèle de turbulence SST k-ω afin d'étudier les phénomènes thermo-hydrodynamiques. Plusieurs paramètres ont été analysés : La distribution de température, le nombre de Nusselt local, le coefficient de frottement, l'énergie cinétique turbulence (TKE) et les lignes de courant.
L'étude paramétrique a porté sur trois paramètres géométriques :
Le nombre d'ailettes, la profondeur des ailettes, l'angle d'inclinaison des ailettes.
Les résultats montrent que l'ajout des ailettes améliore le transfert thermique par rapport au cas sans ailettes grâce à la création de zones de recirculation et à l'amélioration du mélange entre le fluide proche de la paroi et le fluide central. Cependant, une augmentation excessive du nombre d'ailettes, de la profondeur ou de l'angle

d'inclinaison entraîne une augmentation importante des pertes de charge et du coefficient de frottement. Après comparaison des différentes configurations étudiées, la meilleure performance thermo-hydraulique globale est obtenue pour : 5 ailettes, profondeur Dp = 0.5, angle α = 30°

Mot clé : Nombre d'ailette**,** Transfer de chaleur, coefficientent de frottement Nombre de Nusselt, l'énergie cinétique turbulence

Abstract

This thesis presents a numerical study based on the CFD method to analyze the influence of "shark fin" type turbulence-generating fins on heat transfer enhancement in a rotary kiln. The primary objective is to determine an optimal geometric configuration that improves thermal performance while minimizing associated dynamic losses. A two-dimensional numerical model was developed using the SST k-ω turbulence model to investigate thermo-hydrodynamic phenomena. Several parameters were analyzed: temperature distribution, local Nusselt number, friction coefficient, turbulent kinetic energy (TKE), and streamlines. the parametric study focused on three geometric parameters: Number of fins, fin depth, and fin inclination angle. the results show that adding fins enhances heat transfer compared to the finless case by creating recirculation zones and improving mixing between the fluid near the wall and the fluid in the core. However, excessively increasing the number of fins, their depth, or the inclination angle leads to a significant rise in pressure drop and friction coefficient. After comparing the various configurations studied, the best overall thermo-hydraulic performance was achieved with: 5 fins, a depth of Dp = 0.5, and an angle of α = 30°.

Keyword: Number fins, heat transfer, friction coefficient, SST k-ω, Nusselt Number, turbulent kinetic energy (TKE)

Table of Content

General Introduction

The cement industry is among the most energy-intensive industrial sectors, primarily due to the high thermal requirements of clinker production. The rotary kiln is the core unit of this process, where raw materials undergo drying, preheating, calcination, and sintering at temperatures reaching up to 1450 °C. These processes involve complex interactions between gas flow, solid materials, and heat transfer mechanisms, including radiation, convection, and conduction.

Improving the thermal efficiency of rotary kilns is a major challenge, as it directly affects fuel consumption, operational costs, and environmental impact. One approach to enhance heat transfer consists of modifying the internal kiln geometry using devices such as lifters, baffles, and chains. More recently, fins have been proposed as extended surfaces capable of increasing the heat transfer area and improving thermal interaction between the gas phase, kiln wall, and mate-rial bed. However, their effectiveness in high-temperature rotary kilns remains insufficiently explored.

Due to the harsh operating conditions and limited accessibility of industrial kilns, experimental investigations are difficult. Consequently, Computational Fluid Dynamics (CFD) has become an essential tool for analyzing flow behavior and heat transfer in such systems. CFD enables detailed simulation of turbulence, thermal fields, and gas-solid interactions, providing valuable insights into kiln performance.

The objective of this thesis is to investigate the effect of internal fins on heat transfer in a rotary kiln using a CFD-based approach. A comparative analysis is conducted between a conventional smooth kiln and a finned configuration in order to evaluate the impact of fin geometry on temperature distribution and overall thermal performance.

This thesis is organized as follows:

-Chapter 1 presents a comprehensive literature review on rotary kiln operation, heat transfer mechanisms, and existing enhancement techniques.

-Chapter 2 describes the mathematical modeling and governing equations used in the CFD simulations, including turbulence and radiation models.

-The subsequent chapters present the numerical methodology, results, discussion, and conclusions of the study.

CHAPTER I:
Literature Review of Rotary Kiln Heat Transfer

CHAPTER I: Literature Review of Rotary Kiln Heat Transfer

I.1 Introduction

The rotary kiln is the heart of the cement manufacturing process and plays a crucial role in clinker production. It is a long, slightly inclined cylindrical furnace lined with refractory materials and rotating slowly around its axis. The raw meal enters the kiln from the upper end and gradually moves toward the lower end due to the combined effect of gravity.

I.1.1 Definition to Cement Rotary Kilns

Cement manufacturing remains one of the most energy and carbon-intensive industrial activities because clinker production requires both high temperature heat and the calcination of carbonate raw materials. Recent decarbonization literature identifies kiln pyro processing as the central process unit in which thermal efficiency, fuel selection, process control, and heat recovery directly influence total plant energy demand and carbon dioxide emissions [1-2] . The cement rotary kiln is therefore not only a production reactor for clinker formation but also a critical target for energy and emissions reduction.

Figure I.1: Typical cement rotary kiln system

A rotary kiln is a slightly inclined, slowly rotating cylindrical furnace lined with refractory material. Raw meal enters from the upper, colder end of the kiln and moves gradually toward the lower, hotter end as the shell rotates. Combustion gases flow counter currently against the moving solids, creating the main thermal driving force for drying, preheating, calcination, and clinkering. "Modern dry process systems also include cyclone preheaters, precalciners, burners, clinker coolers, induced draft fans, and heat recovery equipment, so the kiln must be analyzed as part of an integrated thermal system rather than as an isolated tube" (Espace_réservé1).

The operating temperature inside a cement rotary kiln normally reaches the clinkering range of approximately 1400 ,1450 °C. At these temperatures, heat transfer is governed by coupled radiation, convection, conduction, bed mixing, gas flow, wall heat storage, shell losses, and chemical reactions. Because direct measurement inside the rotating, dusty, high-temperature environment is difficult, recent studies increasingly use numerical models, discrete ordinates radiation models, CFD, DEM, and dynamic simulation to evaluate kiln performance and design improvements [8–11].

I.2 Operating Principles and Thermal Zones

The transformation of raw meal into clinker occurs through a sequence of temperature dependent physical and chemical processes. Although the exact boundaries depend on kiln design, feed chemistry, fuel type, burner operation, and residence time, the kiln is commonly divided into drying and preheating, calcining, sintering, and cooling regions. These zones are useful for heat transfer analysis because each region has a different dominant mechanism, thermal load, and process objective [5, 6, 10].

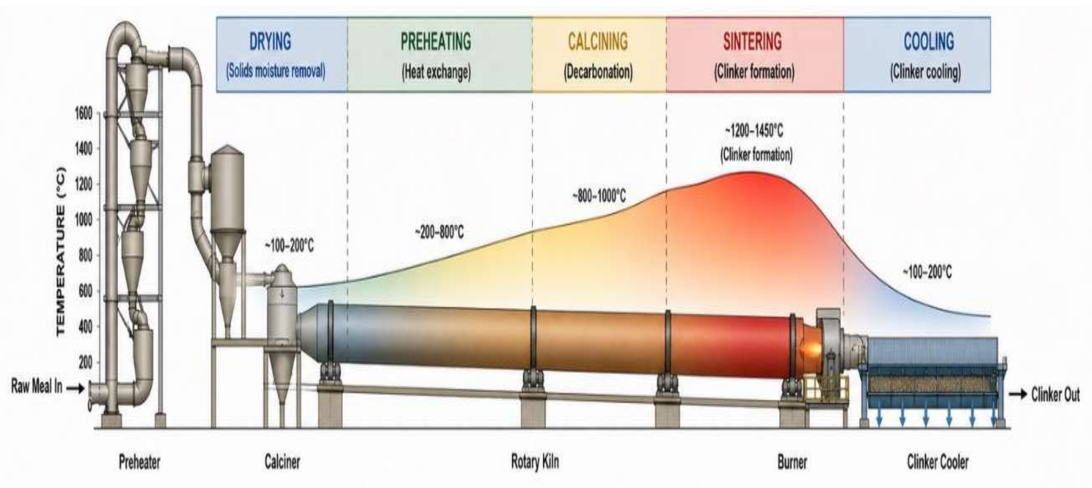

Figure I.2: thermal zone of rotary kiln cement

The drying and preheating zone is located near the feed end of the kiln or, in modern plants, partly upstream in the preheater tower. Moisture is evaporated first, followed by the heating of the solid feed and the release of chemically bound water from clay minerals. In this region, air solid convection is important because the temperature level is lower than in the burning zone, although radiation from hot air and refractory surfaces still contributes to the total heat exchange. Heat recovery from exhaust air is essential because insufficient preheating increases the thermal load imposed on the downstream calcining and clinkering sections [5,7, 9].

I.2.1 Calcination Reactions and Thermal Requirements

The calcining zone is dominated by the endothermic decomposition of calcium carbonate into calcium oxide and carbon dioxide:

$$CaCO_3(s) \rightarrow CaO(s) + CO_2(g). \tag{I.1}$$

Calcination consumes a large fraction of the process heat and strongly affects the gas composition, local heat transfer rate, and residence time requirement. Recent CFD and heat transfer studies on rotary lime and cement kilns show that the prediction of calcination requires simultaneous treatment of air flow, wall to bed exchange, radiation, and reaction kinetics [6, 7, 10]. Incomplete calcination in-creases the load on the sintering zone, while excessive thermal input raises fuel use and may destabilize coating formation and clinker quality.

I.2.2 Sintering Zone and Clinker Formation

After calcination, calcium oxide reacts with silica, alumina, and iron bearing phases to form the principal clinker minerals: alite (C_3S), belite (C_2S), aluminate (C_3A), and ferrite (C_4AF). The sintering zone contains the highest gas and wall temperatures in the kiln, and a partial liquid phase forms to accelerate diffusion and clinker nodule growth. Radiation from the flame, hot gases, and refractory lining becomes the dominant heat transfer mechanism in this zone [8, 12, 13]. The stability of the burning zone is therefore critical for clinker quality, coating behaviors, fuel efficiency, and refractory life.

I.2.3 Clinker Cooling and Heat Recovery

At the kiln discharge, clinker must be cooled rapidly enough to preserve desirable mineral phases and recover sensible heat. In a complete plant model, the clinker cooler is coupled to the rotary kiln because hot secondary and tertiary air from the cooler supports combustion and percaline operation. Recent kiln heat loss studies emphasize that cooler heat recovery, air leakage, wall heat losses, and gas enthalpy losses must be treated together when evaluating overall thermal efficiency [4, 6, 7].

I.3 Heat Transfer Mechanisms in a Rotary Kiln

Heat transfer in a rotary kiln occurs through coupled radiation, convection, and conduction between the gas phase, flame, refractory wall, steel shell, and granular solid bed. The relative importance of these mechanisms changes along the kiln length. Lower temperature zones depend more strongly on convection and
solids mixing, while the calcining and sintering zones require accurate radiation modelling because radiative exchange increases rapidly with absolute temperature [5, 8, 9].

I.3.1 Radiative Heat Transfer Mechanisms

Radiation is the dominant heat-transfer mode in the high temperature regions of the kiln. The flame, combustion gases, suspended particles, and refractory lining exchange radiation with the exposed bed and uncovered wall. Participating gases such as CO_2 and H_2O absorb and emit radiation over wavelength bands, while dust and particles can also scatter and absorb radiant energy. Discrete ordinates models have been used in recent rotary kiln research to resolve radiative exchange in cylindrical and semi cylindrical enclosures with bed material present [6, 8, 13].

I.3.2 Convective Heat Transfer Mechanisms

Convective heat transfer occurs between the moving gas stream and both the exposed bed surface and refractory wall. Its magnitude depends on gas velocity, gas temperature, bed surface renewal, particle exposure, and turbulence. Rotary motion improves convection by disturbing the solid surface and renewing the particles exposed to the gas. Flighted drums, baffles, and built-in structures enhance this mechanism further by increasing the surface area of particles suspended or exposed in the gas phase [14–17].

I.3.3 Conductive Heat Transfer Mechanisms

Conduction occurs through the refractory lining, steel shell, solid particles, and the contact regions between the bed and wall. In granular beds, conduction is limited by particle contacts, voids, and poor internal mixing, so temperature gradients may persist across the bed depth. Infrared thermography and DEM based studies of rotary drums show that wall bed contact, particle residence near heated surfaces, and mixing patterns strongly affect the effective conductive heat transfer inside the solids phase [18–21].

CHAPTER I: Literature Review of Rotary Kiln Heat Transfer

I .4 State of the Art in Heat Transfer Enhancement

Heat-transfer enhancement in rotary kilns and rotary drums is commonly achieved by adding internal structures that increase exposed surface area, intensify bed mixing, extend particle residence in heated zones, or improve wall to bed contact. Recent work focuses on built ins, flights, baffles, and internally heated structures because these elements can redistribute solids and reduce the thermal resistance caused by a poorly mixed granular bed [14, 17, 19, 22, 23].

I.4.1 Lifter and Tumbler Enhancement Systems

Lifters, often called flights, are plates or shelves fixed to the inner surface of a rotary drum or kiln. During rotation, they lift particles from the lower bed and release them through the gas space as particle curtains. This action increases the gas-solid contact area and improves the temperature uniformity of the solid phase. Experimental work on flighted rotary drums confirms that flight geometry, fill degree, rotation speed, and gas,solid operating conditions influence particle distribution and temperature development [15, 16]. DEM studies also show that inclined flight geometry changes particle hold up, axial transport, and active surface renewal, which are directly relevant to kiln heat transfer design [21, 24].

For cement kilns, lifters are most applicable in lower temperature zones because the clinkering zone involves sticky material, coating formation, refractory wear, and severe thermal loading. Therefore, lifters are useful for enhancing convective exchange and mixing in preheating or drying duties, but their use in the hottest sintering region requires careful material and fouling assessment [5, 12].

I.4.2 Chain Systems for Heat Transfer

Chain systems are traditionally used in wet-process and long dry process kilns to increase the heat transfer area in the colder part of the kiln. They absorb heat from the gas stream, transfer heat to the solids by direct contact, and also act as lifting elements. However, chains are limited by wear, breakage, dust accumulation, ring formation, and loss of mechanical strength at elevated temperature. For this reason, modern research attention has shifted toward alternative built ins, baffles, refractory structures, and electrically or indirectly heated rotary designs that can produce stronger and more controllable wall to bed heat transfer [14, 19, 23, 25].

I.4.3 Other Internal Attachments

Other attachments include baffles, refractory projections, trefoil structures, cellular inserts, and internally heated axial elements. The common purpose is to increase solid air exposure, improve solids turnover, or create stronger contact between bed material and heated surfaces. DEM analyses of baffle equipped rotary drums show that baffles can improve heat transfer uniformity and reduce the time required to heat the particle bed, although the outcome depends strongly on baffle height, number, spacing, and particle properties [17, 20, 22, 23]. Electrically heated rotary calciners and plasma heated kilns are also being investigated as possible low carbon configurations, making internal heat transfer design increasingly important for future kiln technology [6, 13, 25].

I.5 Fin Geometries for Heat Transfer Enhancement

Fins provide an extended surface that increases the effective heat transfer area and can conduct heat from a heated wall into a region where the local heat transfer coefficient or thermal conductivity is low. In general heat exchanger

applications, fin performance depends on geometry, thickness, pitch, thermal conductivity, surface efficiency, pressure drop, fouling resistance, and manufactural Bility [26, 27]. These design variables are directly relevant to rotary kiln internals because a fin attached to the refractory or shell facing surface would have to transfer heat while resisting abrasion, chemical attack, thermal cycling, and coating accumulation.

Figure I.3: heat transfer enhancement

Longitudinal fins are aligned with the kiln axis and can increase the wall bed contact area without imposing strong axial forcing. Helical fins wrap around the inner circumference and may combine heat transfer enhancement with modification of solids transport. Pin fins and segmented fins can increase local area and turbulence, but they may also increase pressure drop, particle trapping, and maintenance requirements. Recent baffle and built in studies show that internal protrusions can substantially alter particle circulation and wall to bed exchange, which supports the use of fin like geometries as a plausible enhancement strategy for rotary kilns [14, 19, 21, 23].

The key limitation in applying fins to cement kilns is not the general heat transfer principle but the harsh process environment. Metallic fins may suffer from oxidation, creep, and abrasion in the calcining or sintering zones, while refractory fins must survive thermal shock and mechanical interaction with the moving bed. Consequently, the present research gap is the need to evaluate fin assisted kiln heat transfer under cement kiln relevant temperature, gas, wall, and granular flow conditions rather than relying only on conventional heat exchanger fin correlations [5, 6, 26, 27].

I.6 Computational Fluid Dynamics (CFD) in Kiln Analysis

CFD is widely used in kiln analysis because full field experimental measurement inside an operating cement kiln is difficult, hazardous, and expensive. A CFD model can resolve gas velocity, temperature, turbulence, combustion, species transport, radiation, and wall heat transfer. When coupled with solid bed models, DEM, or dynamic energy balances, it can also estimate bed heating, residence time, and particle scale heat exchange [8–10, 21, 28].

Recent kiln simulations show that the modelling approach must be selected according to the research objective. For air phase combustion and calcination, CFD with radiation and reaction sub models is appropriate [10, 12, 29, 30]. For particle motion, wall bed contact, and internal attachments, DEM or CFD DEM coupling is more suitable because it can capture granular circulation and particle scale heat transfer paths [19–21, 23]. For plant level control and energy analysis, dynamic kiln models and reduced order heat transfer models can be used to study transient response and process optimization [7, 9, 11].

For the present thesis, CFD provides a suitable framework for comparing a baseline kiln with a fin assisted kiln geometry. The key outputs should include air temperature distribution, wall temperature, bed temperature, heat transfer rate, pressure drop, and the uniformity of heat penetration into the solid phase. Because radiation is dominant in the high temperature kiln environment, the CFD model should include a radiation treatment capable of representing air wall bed exchange, while the solid phase should be represented with sufficient detail to evaluate the impact of fins on mixing and wall to bed heat transfer [6, 8, 9, 13].

I.7 Conclusion

This chapter addresses that gap by developing two-dimensional CFD based model to investigate heat transfer enhancement in a cement rotary kiln using internal fins. The study compares the baseline kiln with a fin-assisted configuration and evaluates the effect of the fin geometry on air phase temperature, wall to bed heat transfer, solid-phase heating, thermal uniformity, and overall kiln energy performance. The expected contribution is a clearer technical basis for assessing whether internal fins can improve thermal efficiency in cement rotary kilns while remaining compatible with practical process constrain

CHAPTER II:

Mathematical Modeling and Governing Equations

II.1 Introduction:

This chapter presents the mathematical modeling framework used to investigate heat-transfer enhancement in a cement rotary kiln equipped with internal fins. It continues the same research direction established in Chapter 1, where the rotary kiln was identified as a high-temperature reactor governed by coupled gas flow, wall conduction, radiation, granular-bed heating, and heat losses. The purpose of this chapter is to define the physical domain, simplifying assumptions, governing equations, turbulence model, radiation model, boundary conditions, and dimensionless parameters required for the CFD analysis.

Recent rotary-kiln modeling studies show that CFD can be used to evaluate burner performance, turbulent combustion, flame behavior, thermal fields, and gas-solid heat exchange in rotary-kiln systems [31–34]. For the present work, the mathematical model is formulated for comparative analysis between a baseline smooth kiln and a modified kiln containing internal fins.

II.2 Governing equations:

II.2.1 Conservation Equations for Kiln Flow:

The numerical model is based on the conservation equations of mass, momentum, and energy. These equations describe the velocity, pressure, and temperature fields in the kiln. CFD studies of rotary kilns commonly solve these equations with turbulence and radiation models because the flow is turbulent and the temperature level is high [31, 32, 38].

II.2.2 Mass Conservation Equation Formulation:

The conservation of mass for the gas phase is expressed as

$$\frac{\partial \rho}{\partial t} + \nabla\,(\rho\ \bar{\nabla}) = 0 \qquad \text{(II.1)}$$

where ρ is the gas density and **u** is the velocity vector. For steady-state operation, the time-dependent term is neglected. Because the temperature inside the kiln varies strongly, gas density may be treated as temperature-dependent.

II.2.3Momentum Conservation Equation Formulation:

The momentum equation for the gas phase is written in simplified form as

$$\frac{\partial(\rho \cup)}{\partial t} + \nabla.(\rho \cup \cup) = -\nabla p + \nabla \tau + \rho g \qquad \text{(II.2)}$$

where p is pressure, τ is the viscous stress tensor, and **g** is gravitational acceleration. The fins modify the momentum field by reducing the available flow area, increasing wall interaction, and creating local recirculation zones. These flow changes are important because local velocity and turbulence directly affect convective heat transfer.

II.2.4 Energy Conservation Equation Formulation:

The energy equation is used to calculate the gas temperature field and the heat transferred to the wall, fins, and solid bed. A simplified temperature-based form is

$$\nabla.(\rho Cp \cup T) = \nabla.(Keff \nabla T) + Se \qquad \text{(II.3)}$$

where c_p is the gas specific heat capacity, T is temperature, k_{eff} is the effective thermal conductivity, and S_E is the energy source term. The effective thermal conductivity includes molecular and turbulent contributions.

II.2.5 Source Terms for Heat Transfer:

The source term in the energy equation includes the major heating and cooling effects in the kiln. It may be written as

$$Se = Sheat + Srad + Sbed + Sloss \qquad \text{(II.4)}$$

where S_{heat} represents heat supplied by combustion or imposed inlet heating, S_{rad} represents radiation exchange, S_{bed} represents heat absorbed by the material bed, and S_{loss} represents heat loss through the kiln wall or shell.

For engineering comparison, the convective heat-transfer rate is expressed as

$$Q = hA(Tg - Ts) \qquad \text{(II.5)}$$

where h is the convective heat-transfer coefficient, A is the heat-transfer area,

T_g is the gas temperature, and T_s is the surface temperature. The fins increase A and may also change h by modifying the local flow field.

II.3 Turbulence Modeling for Rotary Kilns:

Turbulence modeling is required because rotary-kiln gas flow is affected by burner momentum, large temperature gradients, buoyancy, wall interaction, and internal geometry. Turbulence increases mixing and influences the convective heat-transfer coefficient. Recent kiln CFD studies commonly use Reynolds-averaged turbulence models because they provide practical accuracy at acceptable computational cost [31–33, 41].

II. 4 Standard K Epsilon Turbulence Model:

The standard $k–\varepsilon$ model is a two-equation turbulence model that solves for the turbulent kinetic energy k and its dissipation rate ε. It is widely used in industrial CFD because it is stable and computationally economical. For rotary-kiln modelling, it can be useful for preliminary simulations and for obtaining an initial flow field However, the model may be less accurate in regions with strong curvature, separation, swirl, and adverse pressure gradients. These limitations are relevant when internal fins are installed because fins create local flow disturbance and near-wall recirculation.

II.4.1 RNG k–ε model:

The transport equations have the same structure as the standard model, but the constants are derived analytically rather than empirically, and an additional source term is introduced in the ε equation to account for the rapid distortion of the turbulence. It usually improves the prediction of separated and swirling flows compared with the standard k–ε model.

II.4.2 Realizable k–ε model:

It is built on a new formulation of the turbulent viscosity and on a new transport equation for ε derived from an exact equation for the mean-square vorticity fluctuation. It satisfies certain mathematical constraints on the Reynolds stresses (realizability), which improves the prediction of round jets, flows with strong streamline curvature and flows with separation.

II.4.3 K Omega Shear Stress Transport Model:

The $k–\omega$ shear stress transport model combines the near-wall accuracy of the $k–\omega$ model with the free-stream robustness of the $k–\varepsilon$ model. This makes it suitable for simulations where wall heat transfer, flow separation, and local recirculation are important. In the present study, the $k–$

ω SST model is recommended for the main CFD simulations because the fins operate in the near-wall region and the accuracy of wall heat-transfer prediction is important.

II.5 Selected Turbulence Model Justification:

The selected turbulence model for the main simulation is the k–ω SST model. This choice is based on the importance of near-wall heat transfer around the fins

and the kiln wall. The standard k–ε model may be used for preliminary simulations, while the Reynolds Stress Model may be used only if strong anisotropic turbulence is observed.

II.6 Thermal Radiation Modeling Approach:

Thermal radiation is a dominant heat-transfer mechanism in rotary kilns because the gas, wall, flame region, and solid bed operate at high temperature. Radiation modeling is especially important in cement-kiln analysis because carbon dioxide, water vapors, particles, and combustion products participate in radiative exchange. Recent high-temperature kiln studies emphasize that gas radiation and non-grey effects may become significant when modelling hydrogen flames, thermal plasmas, and oxy-combustion processes [31, 34, 50].

II.6.1 P One Radiation Model:

The P1 radiation model treats radiation in a diffusion-like form. It is simple, robust, and computationally efficient. It may be useful for preliminary calculations or optically thick media. However, it is less accurate when radiation is strongly directional or when internal fins create shadowing effects. for the present problem, the P1 model is not selected as the main radiation model because the finned geometry requires better treatment of directional radiative exchange.

II.6.2 Discrete Ordinates Radiation Model:

The Discrete Ordinates radiation model solves the radiation field over a finite number of angular directions. It can represent directional radiation, participating gases, and complex internal geometry. This makes it suitable for a kiln with fins, where surfaces may block, reflect, or redirect radiative heat transfer. the Discrete Ordinates model is therefore selected for the main radiation calculation. It is more computationally expensive than the P1 model, but it is better suited to high-temperature kiln simulation with internal structures.

II.6.3 Surface to Surface Radiation Model:

The Surface-to-Surface radiation model calculates radiative exchange between solid surfaces using view factors. It is suitable when the gas between the surfaces is non participating. In cement kilns, however, the gas phase normally contains radiating species and suspended particles, so the Surface-to-Surface model is not sufficient for the full domain. it may still be useful for simplified comparisons of wall-fin-bed radiation if gas radiation is neglected.

II.6.4 Selected Radiation Model Justification:

The selected radiation model is the Discrete Ordinates model. This choice is justified by the high operating temperature, the presence of participating gases, and the geometric complexity caused by internal fins. Gas radiation-property models, such as grey-gas or weighted sum of grey gases approaches, may be required when detailed gas composition is available [50].

II.6.5 Initial Temperature and Flow Conditions:

For steady-state simulations, initial conditions are used to start the iterative solution. A uniform initial temperature may be used for simple cases, but an approximate axial temperature profile can improve convergence. For transient simulations, the initial conditions represent the physical state of the kiln at the beginning of the calculation the initial velocity field may be set to zero or initialized using the inlet velocity. The initial temperature field should be chosen carefully because rotary kiln simulations involve strong coupling between radiation, convection, and wall conduction.

II.7 Dimensionless Numbers for Heat Transfer Analysis:

Dimensionless numbers are used to compare kiln operating conditions and geometry modifications. In this study, Reynolds number, Prandtl number, and Nusselt number are used to characterize flow and heat transfer behavior. These numbers are also useful for comparing the baseline smooth kiln with the fin-assisted kiln.

II.7.1 Reynolds Number Flow Characterization

The Reynolds number describes the ratio of inertial forces to viscous forces:

$$Re = \frac{\rho * U * Dh}{\mu} \tag{II.6}$$

where D_h is the hydraulic diameter and μ is the dynamic viscosity. A high Reynolds number indicates turbulent flow. Internal fins can modify the effective hydraulic diameter and local velocity field.

II.7.2 Prandtl Number Thermal Characterization:

The Prandtl number describes the ratio of momentum diffusivity to thermal diffusivity:

$$Pr = \frac{\mu * Cp}{k} \tag{II.7}$$

For gases, the Prandtl number is usually close to unity. It affects the relative thickness of the velocity and thermal boundary layers and therefore influences convective heat transfer.

II .7.3 Nusselt Number Heat Transfer Characterization:

The Nusselt number expresses the strength of convective heat transfer relative to conduction:

$$Nu = \frac{h * Dh}{K} \tag{II.8}$$

A higher Nusselt number indicates stronger convective heat transfer. In the present thesis, the Nusselt number is used to compare the smooth kiln and the fin assisted kiln. Recent heat transfer enhancement studies use Nusselt number and heat-transfer coefficient evaluation to quantify the effect of grooves, flights, and other internal structures [41, 43, 44].

II .8 conclusion

This chapter defines the mathematical modeling framework for the CFD analysis of a cement rotary kiln equipped with internal fins. The physical domain consists of a cylindrical kiln, gas freeboard, lower solid-bed region, refractory wall, and internal fin structures. The baseline case represents a smooth kiln, while the modified case contains internal fins intended to increase heat-transfer area and improve air wall bed thermal interaction the governing equations are the conservation equations of mass, momentum, and energy.

CHAPTER III: NUMERICAL METHODS

CHAPTER III: NUMERICAL METHODS

III.1 Introduction

Industrial rotary kilns (cement, lime, metallurgy) are highly energy intensive devices. They host complex, strongly coupled physical phenomena: a turbulent diffusion flame, convective and radiative heat transfers, a moving granular bed, and specific internal geometries. Due to extreme conditions (temperatures exceeding 1700 K, rotation, dust) and safety constraints, direct full-scale experimentation is virtually impossible. Consequently, Computational Fluid Dynamics (CFD) has become the standard tool to analyze, optimize, and virtually test design modifications (burners, secondary air, geometry) in a non-intrusive, cost effective, and repeatable manner.

III.2Finite Volume Method

III.2.1Definition

The Finite Volume Method (FVM) is a numerical technique that converts the partial differential equations governing the conservation of mass, momentum, energy and chemical species into a system of algebraic equations defined on a discrete partition of the physical domain. The strength of the method, and the main reason for its prevalence in industrial CFD, lies in the fact that the discretization is performed directly on the integral (conservative) form of the governing equations. As a consequence, the fluxes that enter a control volume through one of its faces are identical, but with opposite sign, to the fluxes leaving the neighboring control volume through the same face. Mass, momentum and energy are therefore conserved exactly at the discrete level, even on course meshes a property that is essential when long simulation times or strongly non-linear phenomena such as combustion are involved.

The physical domain Ω is divided into a finite number of contiguous, non-overlapping control volumes Vi, often referred to as cells. A general conservation equation for an intensive transport variable φ (which can stand for the velocity components, the enthalpy, the mass fraction of a chemical species, the turbulent kinetic energy, and so on) is written as:

$$\partial(\rho\varphi),\partial t \ + \ \nabla\cdot(\rho\, \boldsymbol{u}\, \varphi) \ = \ \nabla\cdot(\Gamma\, \nabla\varphi) \ + \ S_\varphi \qquad \text{(III.1)}$$

where ρ is the density, u the velocity vector, Γ a generalized diffusion coefficient, and S φ a volumetric source term that gathers all contributions that are not pure convection or pure diffusion (e.g. pressure gradients, body forces, chemical reaction, radiative absorption). Integrating Eq. (III.1) over a control volume Vi and applying the divergence theorem yields the balance equation actually solved by the FVM:

$$\partial,\partial t \ \int_V \rho\varphi \, dV \ + \ \oint_S \rho\varphi \ \boldsymbol{u}\cdot\boldsymbol{n} \, dS \ = \ \oint_S \Gamma\, \nabla\varphi\cdot\boldsymbol{n} \, dS \ + \ \int_V S_\varphi \, dV \qquad \text{(III.2)}$$

The volume integrals are then approximated by the value of the integrand at the cell centroid multiplied by the cell volume, while the surface integrals are evaluated face by face. The convective and diffusive fluxes through each face require the value of φ and of its gradient at the face Centre; these are reconstructed from the cell-centered values by means of an interpolation scheme. In the present work, a second-order upwind scheme is used for the convective terms in order to limit numerical diffusion in the flame region, and a central scheme is used for the diffusive terms. The pressure–velocity coupling is treated by the SIMPLE algorithm of Patankar, which is the default choice in Fluent for steady, incompressible or weakly compressible flows.

The discretization procedure transforms Eq. (III.2), originally a partial differential equation, into a sparse linear algebraic system of the form $A \cdot \Phi = b$, where the vector Φ collects the unknown cell-centered values of φ. The matrix A is sparse because each row links only one cell to its immediate neighbors, and the system is solved iteratively using an algebraic multigrid solver. The solution is considered converged when the scaled residuals fall below a prescribed threshold (typically 10^{-4} for the continuity and momentum equations, and 10^{-6} for the energy equation) and when the integral quantities of interest, such as the outlet mass flow rate, the outlet temperature and the wall heat flux, become stationary.

III.2.2 Three properties summarize why FVM is particularly well suited to industrial combustion problems such as the present rotary kiln study:

- Local and global conservation: mass, momentum, energy and species are conserved exactly, both cell-by-cell and over the whole domain, regardless of the mesh quality.
- Geometric flexibility: any cell shape (hexahedral, tetrahedral, polyhedral, prismatic) is acceptable, which makes it possible to capture the burner, the shark fins and the inclined kiln shell with the same algorithm.
- Direct treatment of boundary conditions: Dirichlet, Neumann and mixed boundary conditions are applied directly to the face fluxes, ensuring that wall heat flux, mass flow rate and pressure outlet conditions are imposed in a strictly conservative manner.

III.3 Presentation of ANSYS ICEM CFD

ANSYS ICEM CFD is the pre-processor used in this work to generate the computational domain and the volume mesh that will subsequently be loaded into the solver. It is a multi-purpose geometry and meshing environment that can either import CAD geometries from external systems (STEP, IGES, Parasolid, CATIA, SolidWorks, etc.) or build them from

scratch through its own geometry kernel. The user organizes the model in a hierarchical tree composed of points, curves, surfaces and bodies, and groups them into named ‘parts’ that are later used by Fluent to identify boundary conditions. For the kiln configurations studied here, ICEM CFD was used in two complementary modes. The geometry of the kiln, the burner, the secondary-air openings, the shark fin inserts and the outlet section was created directly inside the geometry workbench by combining elementary operations on points, curves and surfaces. A blocking strategy was then defined on top of the geometry, in order to obtain a structured (multi-block hexahedral) mesh. This approach guarantees a high level of alignment between the mesh and the dominant flow direction, which is decisive for the accuracy of convective transport in elongated devices such as kilns. Wherever the geometric complexity (in particular around the shark fins) made a fully structured discretization impractical, the structured blocks were combined with an unstructured tetrahedral mesh and the transition between the two zones was smoothed by means of pyramidal elements.

After mesh generation, the quality of the elements was systematically checked using the built-in diagnostics of ICEM CFD. Three indicators were monitored: the equivolume skewness (kept below 0.85 in the entire domain and below 0.6 over more than 95 % of the cells), the aspect ratio (kept below 50 in the wall-attached layers and below 10 elsewhere), and the orthogonal quality (kept above 0.20). Cells that did not satisfy these criteria were either manually corrected by editing the underlying block topology or smoothed using the Laplace smoother of ICEM CFD. The mesh is finally exported to the . mesh format directly readable by Fluent.

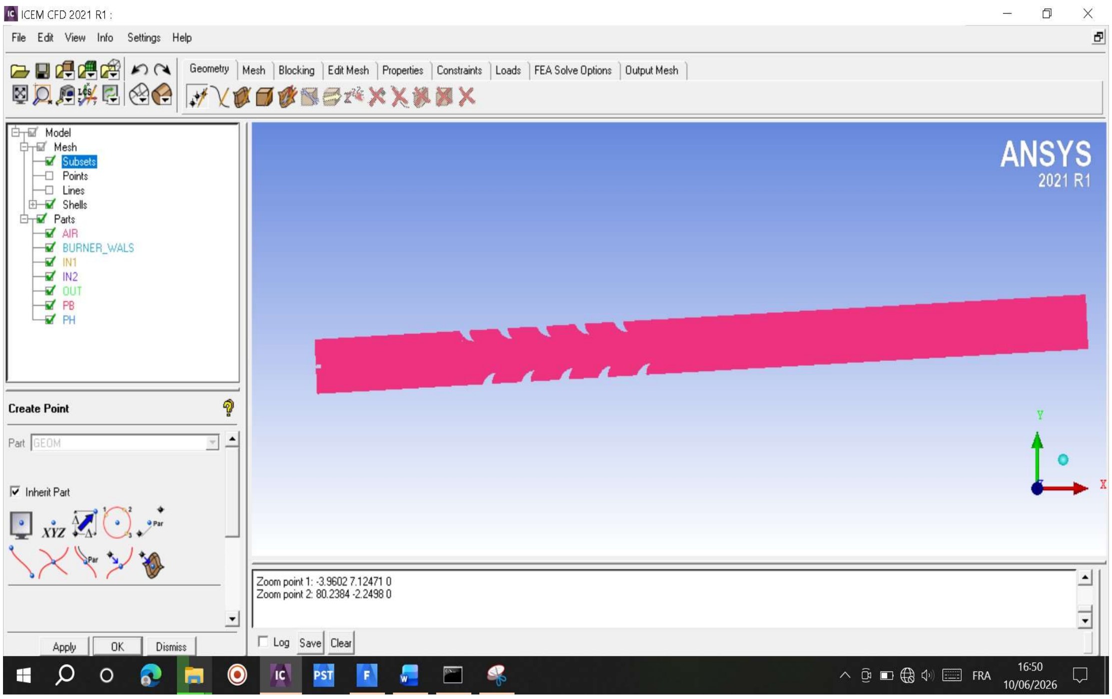

Figure III.1 ANSYS ICEM CFD 2021 R1 working environment showing the kiln geometry and the named parts used to identify the boundary conditions.

Figure III.1 shows the ICEM CFD interface during the pre-processing stage of the present study. The model tree on the left lists the geometric entities and the named parts (AIR, BURNER_WALS, IN1, IN2, OUT, PB, PH) which will receive specific boundary conditions in the solver. The graphics window displays the kiln shell with the shark-fin inserts protruding from the upper and lower walls.

III.4 Presentation of ANSYS Fluent 21

ANSYS Fluent is the CFD solver used in this work to integrate the governing equations on the mesh produced by ICEM CFD. Fluent is a general-purpose, finite-volume code that includes a wide library of physical models: incompressible and compressible flow, laminar and turbulent regimes, single- and multi-phase flows, conjugate heat transfer, gaseous and particle combustion, surface and volumetric chemical reactions, radiation, and a comprehensive set of turbulence closures. The version used for the present simulations is ANSYS Fluent 2021 R1, in its double-precision pressure-based mode (PBNS) running in parallel on a multi-core workstation.

Once the mesh has been read into Fluent, the user follows the natural top down workflow visible in the Outline View shown in Figure III.2: General (units, solver type, gravity), Models (energy, viscous model, radiation, species transport), Materials (fluid and solid properties), Cell Zone Conditions (fluid zones, porous media, solid zones), and Boundary Conditions (inlets, outlets, walls). Each of these tabs gives access to the parameters that are relevant for industrial combustion: the choice between standard k–ε, RNG k–ε, Realizable k–ε or SST k–ω for the turbulence model; the choice between the P-1, the Discrete Ordinates (DO) and the Rosseland models for radiation; the choice between species transport, Non Premixed Combustion (PDF), Premixed Combustion or Partially Premixed Combustion for the chemistry.

Figure III.2 corresponds to the configuration of the kiln equipped with shark fins, with a two-dimensional pressure based, steady solver activated. The boundary list on the left of the Outline View identifies the walls of the burner (burner wall, id 14), the two secondary air openings (in1, id 12 and in2, id 13), the pressure outlet (out, id 15) and the porous brick wall section (pb, id 16). This labelling is exactly the one transmitted from ICEM CFD through the named parts of Figure III.1.

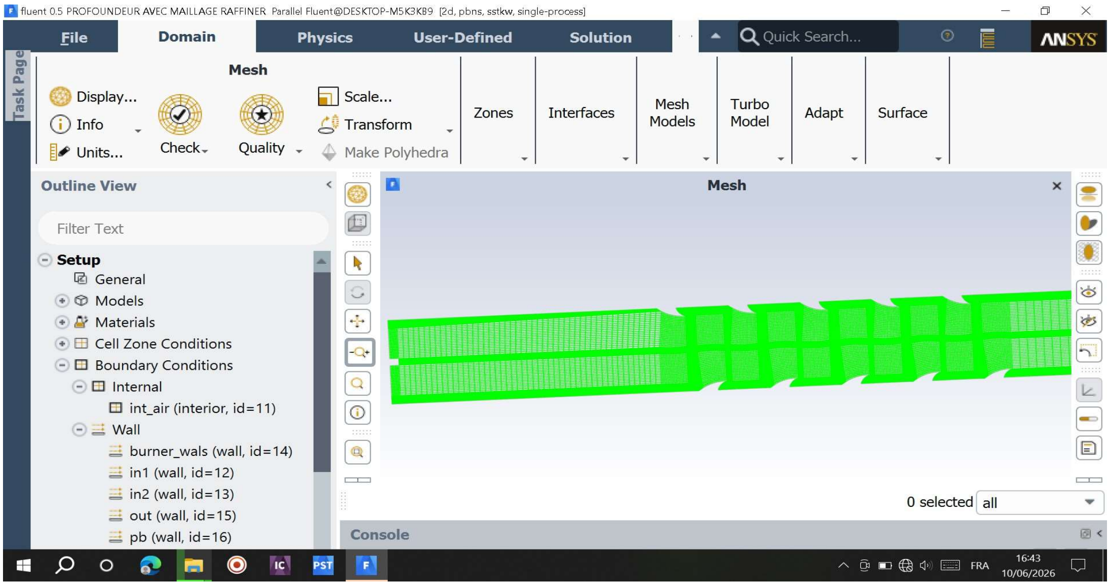

Figure III.2 ANSYS Fluent 2021 R1 working environment showing the imported mesh, the Outline View tree (General → Models → Materials → Cell Zone Conditions → Boundary Conditions) and the labelled boundaries used in the present simulations.

From the numerical point of view, the simulations have been carried out with the following settings: pressure-based steady solver; SIMPLE pressure velocity coupling; second-order upwind scheme for the momentum, energy, species and turbulence transport equations; scheme for the pressure (which is well adapted to flows with strong density gradients such as those induced by combustion); least-squares cell-based gradient evaluation. The under-relaxation factors were progressively reduced from their default values during the first iterations in order to stabilize the solution, and they were restored to the default values once the residuals started decreasing monotonically.

III.5 Case Study

The case study addressed in this thesis is an industrial rotary kiln of the type commonly encountered in cement and lime production. Two configurations are simulated and compared: a baseline (smooth) configuration in which the inner surface of the kiln is geometrically uniform, and a modified configuration in which a set of shark-fin lifters is mounted on the upper and lower walls of the kiln in order to enhance the mixing between the flame, the secondary air and the granular charge. The objective of this comparison is to evaluate how the presence of the fins modifies the velocity, temperature and species fields, and ultimately the thermal performance of the kiln.

III.6 Geometry

The geometry retained for the simulations reproduces the main proportions of a typical industrial cement rotary kiln operating in a dry process. The kiln is modelled as an inclined cylindrical shell of length L and internal diameter D kiln, fed at the upstream end by a central axial burner of diameter d burner surrounded by two annular openings dedicated to the secondary combustion air. The shell is inclined at an angle α with respect to the horizontal plane, which corresponds to the natural slope used in practice to convey the granular charge by gravity from the inlet (raw meal feed) to the outlet (clinker discharge).

Figure III.3 illustrates the modified configuration. Eight shark-fin lifters are mounted on the inner surface of the kiln, four on the upper wall and four on the lower wall, with a longitudinal pitch that distributes them along the active combustion zone (i.e. between and re-injects fluid parcels from the boundary layer into the core of the flame, enhancing the mixing without introducing any mechanical or moving part. This is the geometric idea borrowed from the biomimetic literature on shark skin denticles.

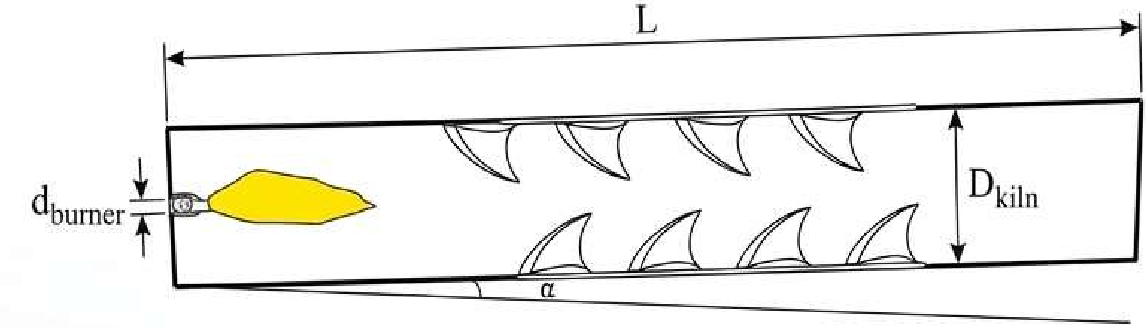

Figure III.3 Geometry of the rotary kiln equipped with shark-fin lifters: kiln length L, internal diameter D kiln, burner diameter d burner and inclination α.

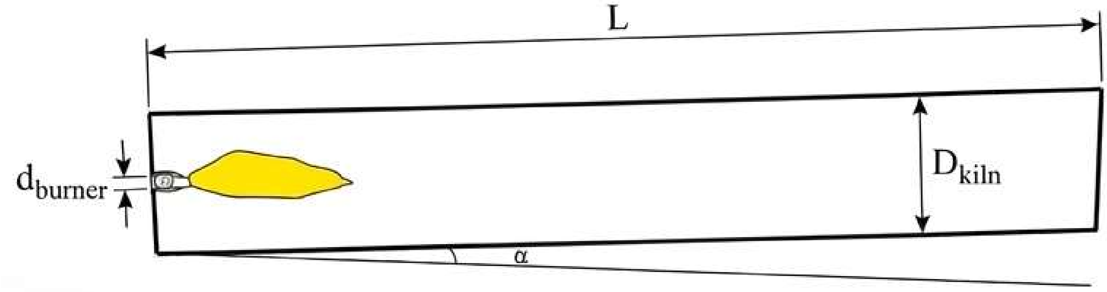

Figure III.4 Geometry of the reference (smooth) rotary kiln, without internal lifters.

Figure III.4 shows the baseline (reference) configuration. The internal surface of the kiln is geometrically smooth: no fin and no lifter is present, and the only feature of the inner geometry is the burner tip protruding from the upstream wall. This configuration is used as the reference case against which the performance of the finned kiln will be evaluated.

The yellow region depicted close to the burner exit on both figures schematically represents the expected position and shape of the diffusion flame issuing from the central burner; the burner is fed with a fuel jet at high velocity and a coaxial primary air stream, while a much larger mass flow rate of secondary air enters through the two annular openings

around the burner. The relative proportions and the inclination angle α have been preserved on the figures, although the longitudinal scale is compressed for readability.

III.7 Boundary Conditions

The boundary conditions are imposed in Fluent on the named surfaces transmitted from ICEM CFD. They translate, at the limits of the computational domain, the physical conditions imposed by the operating point of the kiln. Figure III.5 and Figure III.6 summarize schematically the type of boundary applied to each surface for the two configurations studied. Table 3.2 collects the numerical values associated with the boundaries.

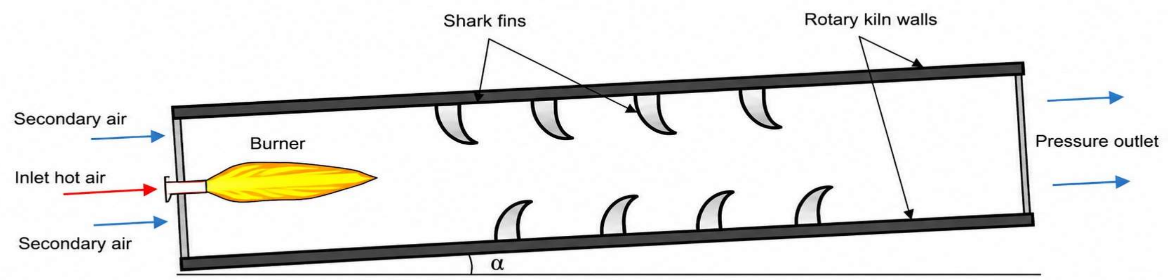

Figure III.5 Boundary conditions applied to the finned kiln configuration: inlet hot air (burner), secondary air on both sides of the burner, shark-fin lifters as no-slip walls, rotary kiln walls and pressure outlet.

III.7.1 Inlet hot air (burner):

The central inlet, located at the burner tip, is modelled as a velocity inlet. The primary stream carries the gaseous fuel (natural gas, modelled as methane CH_4 in the species transport approach, or as a fuel stream of given mixture fraction in the non-premixed approach) and a fraction of the combustion air at high velocity. The inlet velocity, temperature and turbulent quantities (turbulent intensity I = 10 %, hydraulic diameter equal to d_burner) are imposed according to the operating point of the kiln. The mass flow rate of the burner stream is calibrated to deliver the nominal thermal power of the kiln.

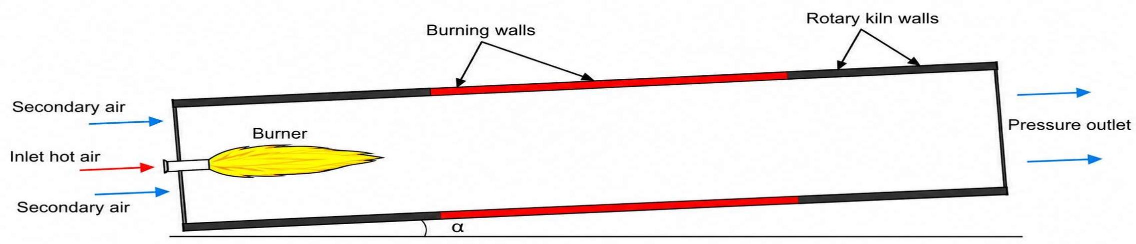

Figure III.6 Boundary conditions applied to the reference (smooth) configuration: same inlets and outlet

III.7.2 Secondary air inlets (in1 and in2):

The two annular openings around the burner are modelled as velocity inlets supplying preheated secondary air, typically recovered from the clinker cooler in an industrial cement plant. The inlet temperature is set to a value representative of the clinker cooler exhaust (≈ 800–1000 K in industrial practice), and the velocity is computed from the required air-to-fuel ratio. Turbulence intensity is set to 5 %.

III.7.3 Pressure outlet (out):

The downstream section, where the flue gases leave the kiln before entering the preheater tower, is modelled as a pressure outlet at the gauge pressure −50 Pa, which reproduces the slight depression imposed by the induced-draught fan of the plant. The backflow temperature and the backflow species composition are set so that, in case of local reverse flow, the boundary values remain physically consistent with the gases expected at the outlet.

III.7.4 Rotary kiln walls:

The cylindrical shell of the kiln is modelled as a no slip stationary wall. In Figure III.6, the wall is subdivided into two parts: a refractory-lined burning zone (highlighted in red), on which a mixed thermal condition is imposed (a prescribed external temperature combined with an equivalent overall heat-transfer coefficient through the refractory), and a non-burning region downstream, treated as adiabatic in a first approximation. In the finned configuration of Figure III.5, the shark fins themselves are stationary no-slip walls coupled by conduction to the kiln shell.

III.7.5 Burner walls (burner_wals):

The metallic walls of the burner lance are treated as adiabatic no-slip walls, which is acceptable here because the burner is short and well insulated relative to the residence time of the gases.

Boundary	Fluent type	Thermal condition
Burner inlet	velocity-inlet	Fixed T primary hot air)
Secondary air 1 (in1)	velocity-inlet	Fixed T (preheated air)
Secondary air 2 (in2)	velocity-inlet	Fixed T (preheated air)
Outlet	pressure-outlet	Backflow conditions
Refractory (burning zone)	wall (no-slip)	Mixed (T_ext, h_overall)
Other kiln walls	wall (no-slip)	Adiabatic
Shark fins	wall (no-slip)	Coupled to shell
Burner walls	wall (no-slip)	Adiabatic

Table III.1 Summary of the boundary conditions imposed on the computational domain.

III.8 Mesh Study

The construction of the mesh is one of the most decisive steps in a CFD analysis: a poor mesh will degrade the accuracy of the solution regardless of the sophistication of the physical models employed. For the present study, particular attention has been paid to two zones of the domain that are particularly demanding in terms of mesh resolution. The first is the near-wall region of the kiln shell and of the shark fins, where the steep velocity and temperature gradients of the boundary layer must be captured. The second is the burner-jet region and the primary reaction zone of the flame, where the chemical reaction takes place and where the highest temperatures and the strongest density gradients are observed.

A multi-block structured strategy was therefore privileged in ICEM CFD. The bulk of the kiln is meshed with hexahedral cells aligned with the longitudinal axis, with a refinement towards the walls that produces an inflation layer of about 12 prismatic-shaped cells. The first cell-Centre height was chosen so that the dimensionless wall distance y^+ remains below 5 in the near-wall region when the enhanced wall treatment is used in Fluent, and between 30 and 300 when standard wall functions are used. Around the shark fins, the block topology is locally refined: the cell size at the fin tip is approximately one tenth of the cell size in the core

of the kiln, with a smooth growth ratio of 1.2 between adjacent cells in order to avoid abrupt size jumps.

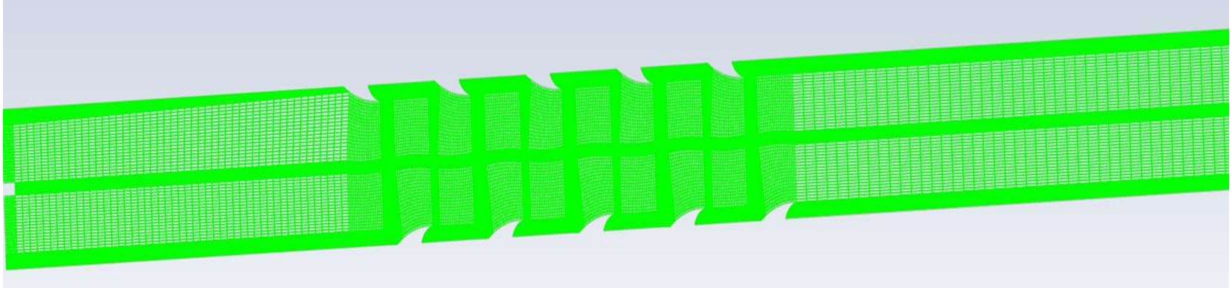

Figure III.7 Volume mesh of the finned configuration. The structured hexahedral mesh is aligned with the kiln axis and is locally refined around each shark-fin lifter.

Figure III.7 shows the resulting mesh in the finned configuration. The streamwise alignment of the hexahedral cells is clearly visible in the bulk region, while the local refinement around the fins is necessary to capture the recirculation bubbles generated downstream of each fin. Figure III.8 shows the mesh on the reference (smooth) configuration: in the absence of internal protrusions, the mesh is essentially a regular hexahedral grid stretched towards the walls.

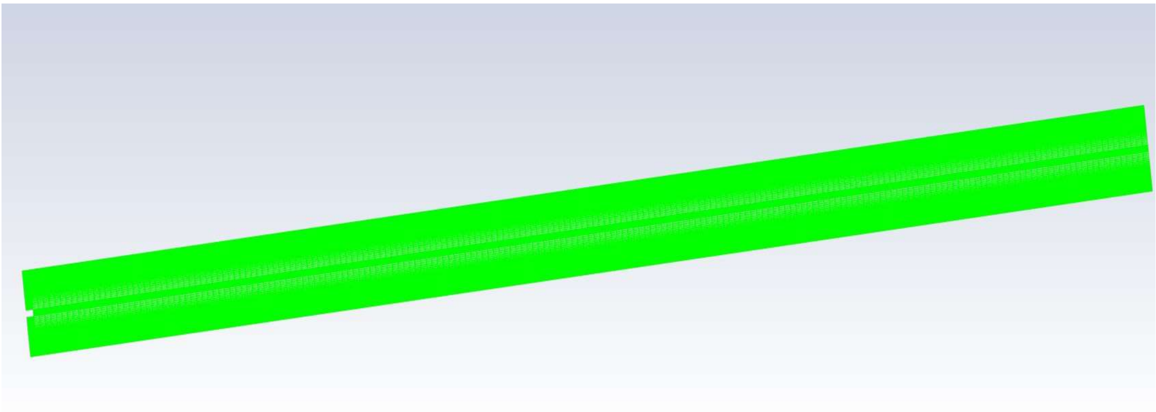

Figure III.8 Volume mesh of the reference (smooth) configuration. The mesh is a regular structured hexahedral grid stretched towards the kiln walls.

A close-up view of the mesh in the fin region (Figure III.9) shows that the orthogonality of the cells is preserved even across the abrupt change of curvature induced by the fin geometry, which is a strong indicator of the quality of the underlying block topology. The mesh quality indicators reported by ICEM CFD for the finned configuration are: minimum determinant 0.41, maximum equi-volume skewness 0.78, and minimum orthogonal quality 0.32, all well above the recommended thresholds for second-order RANS simulations.

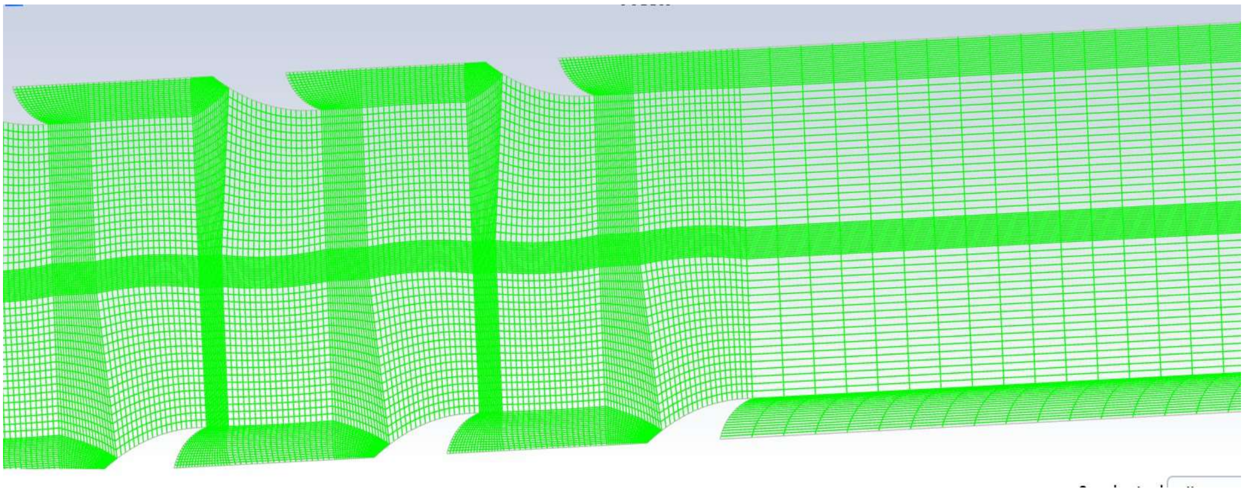

Figure III.9 Close-up view of the structured mesh around two consecutive shark-fin lifters. The local refinement and the orthogonal alignment of the cells are visible.

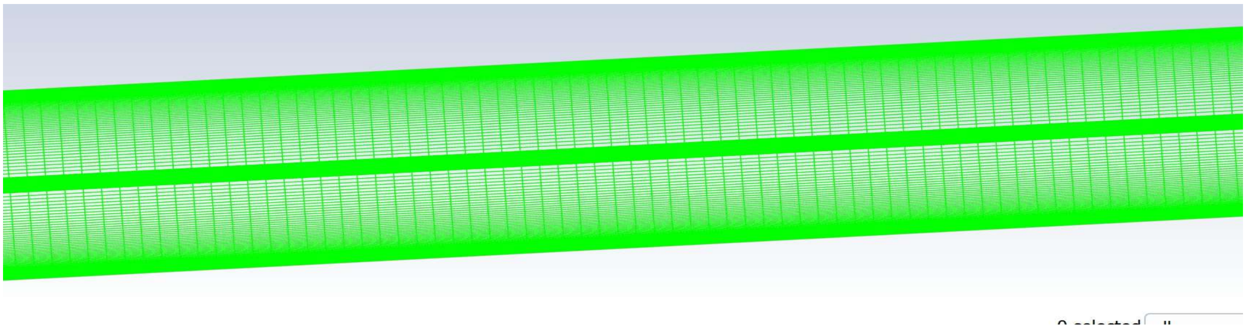

Figure III.10 Close-up view of the near-wall mesh on the reference configuration: the inflation layer is clearly visible against the kiln shell.

III.8.1 Mesh Sensitivity Study

A grid-independence study is mandatory in any rigorous CFD analysis: it ensures that the numerical solution converges towards a unique, mesh-independent result as the size of the cells is progressively reduced. Three meshes of increasing density were generated for the present case and used to compute the same operating point with identical boundary conditions and the same physical models (SST k–ω turbulence closure, P-1 radiation, non-premixed combustion). The characteristics of the three meshes are summarized in Table III.2.

Mesh	Number of nodes	Refinement	Use
Grid 1	30 000	Coarse	Trend , fast tests
Grid 2	60 000	Medium	Reference grid
Grid 3	1 200 000	Fine	Independence check

Table III.2 Meshes used for the grid-independence study.

For each mesh, the axial profile of the temperature along the central line of the kiln (from the burner outlet, x = 0 m, to the kiln exit, x = 40 m) has been extracted from the converged solution and is plotted in Figure 3.11. The temperature was selected as the indicator of the grid-independence because it is the variable of primary engineering interest, and because it is highly sensitive both to the mixing in the near-burner region and to the radiative exchange with the walls further downstream.

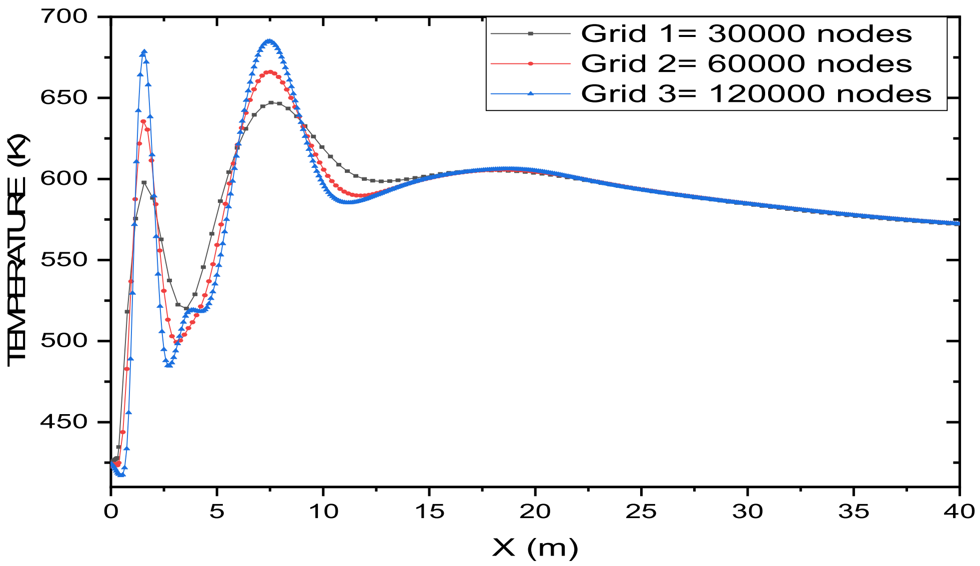

Figure III.11 Axial temperature profile along the kiln centerline for the three meshes (Grid 1: 30 000 nodes; Grid 2: 60 000 nodes; Grid 3: 1 20 000 nodes). Computations performed with the SST k–ω turbulence closure.

Three regions can be identified on Figure 3.11. The first one extends from the burner exit to x ≈ 3 m and is characterized by a sharp temperature peak immediately downstream of the burner, followed by a steep drop associated with the entrainment of the cold secondary air. In this region the three meshes give noticeably different profiles: the coarsest mesh (Grid 1, 30 000 nodes) underestimates both the maximum (~ 645 K instead of ~ 680 K predicted by the two finer grids) and the depth of the subsequent minimum (~ 520 K against ~ 490 K). This is a direct consequence of the excessive numerical diffusion introduced by the coarse cells in the highly sheared mixing layer between the fuel jet and the secondary air. The second region, between x ≈ 3 m and x ≈ 12 m, is the primary combustion zone, where the temperature reaches a second, broader maximum (≈ 680 K for Grids 2 and 3) corresponding to the main heat release of the flame. The agreement between the medium grid (60 000 nodes) and the fine grid (1 20 000 nodes) is already good in this region; the residual difference on the peak value is of the order of 1–2 % only.

Beyond x ≈ 12 m, the three profiles collapse onto a single curve that smoothly decays from ≈ 605 K at the end of the combustion zone to ≈ 570 K at the kiln outlet. This convergence indicates that, far from the burner, the solution is essentially controlled by the convective transport of the hot gases and by the radiative exchange with the kiln walls, two phenomena that are well captured even by the coarse mesh. On the basis of this analysis, Grid 2 (60 000 nodes) has been retained as the working mesh for the rest of the study. It provides a satisfactory compromise between accuracy and computational cost: the relative discrepancy with respect to the finest grid is lower than 3 % on the peak temperature and lower than 1 % on the kiln outlet temperature, while the CPU time per converged simulation is reduced by approximately a factor of 20 with respect to Grid 3. Grid 3 will be used punctually as a reference to confirm the conclusions on the comparison between the smooth and the finned configurations.

III.9 Turbulence models comparison

The choice of the turbulence closure is the second methodological decision that must be made before producing the engineering results of the next chapter. The flow inside an industrial rotary kiln combines a strong axial jet issuing from the burner, large recirculation zones generated either by the burner geometry or by the shark fins, a swirling motion induced by the rotation of the shell, and a strongly inhomogeneous density field induced by combustion. None of the standard two-equation closures has been designed to handle all of these phenomena simultaneously, so the selection of the most appropriate model must be based on a comparative study performed on the case of interest.

Four two-equation RANS closures, all available in Fluent and all commonly used in industrial combustion studies, have been considered:

All four models have been used to simulate the same operating point of the finned kiln, with identical mesh (Grid 2), identical boundary conditions, identical combustion model (non-premixed combustion, equilibrium chemistry) and identical radiation model (P-1). The only thing that has been changed is the turbulence closure. Figure 3.12 reports the resulting axial temperature profile along the kiln centreline for each model.

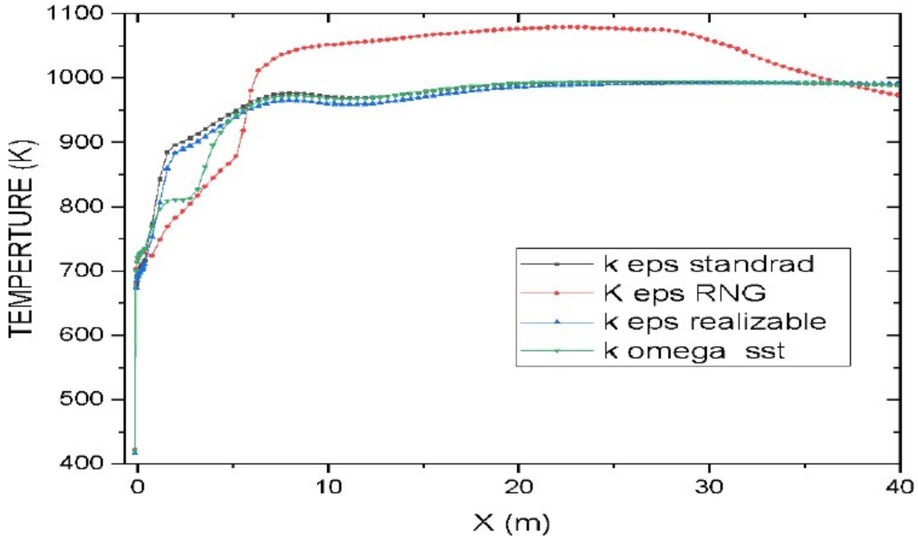

Figure III.12 Axial temperature profile along the kiln centreline obtained with the four turbulence closures (standard k–ε, RNG k–ε, Realizable k–ε and SST k–ω). Same mesh, same boundary conditions and same physical models in all four cases.

Three groups of curves can be identified on Figure 3.12. The first group is made up of the standard k–ε, the Realizable k–ε and the SST k–ω predictions. These three curves are essentially superimposed beyond x ≈ 10 m and they all predict, in the far field, an outlet temperature close to 990 K. The differences between these three closures are confined to the near-burner region (x < 5 m), where the SST k–ω model predicts a slightly slower temperature rise consistent with its known behavior on confined jets, where the SST limiter prevents the spurious overproduction of eddy viscosity in regions of strong shear, and therefore preserves the integrity of the jet over a longer distance.

The second group is reduced to the single RNG k–ε prediction, which systematically overestimates the temperature in the combustion zone by 80 to 100 K (peak value ≈ 1080 K against ≈ 990 K for the other three closures). This systematic deviation is consistent with observations reported in the open literature on diffusion flames: the additional source term in the RNG ε equation reduces the turbulent dissipation in regions of high strain rate, which in turn increases the turbulent viscosity, accelerates the mixing between fuel and oxidizer, and produces a hotter and shorter flame. In the absence of an experimental reference on the present geometry, this excessive sensitivity to the strain rate is considered as a defect rather than as a physically grounded prediction.

The third behavior observed in the very-near-burner region is the slight depression predicted by the SST k–ω model around x ≈ 3 m, which is associated with the better resolution of the recirculation bubble immediately downstream of the burner tip. This is exactly the kind of separated, adverse-pressure-gradient feature for which the SST k–ω model was originally developed, and it is reasonable to consider that this prediction is qualitatively more reliable than the smoother profiles obtained with the k–ε family.

On the basis of these arguments, the SST k–ω model has been retained as the turbulence closure for the rest of the work, for the following three reasons: (i) it is the only closure that behaves correctly both in the near-wall region (down to $y^+ \approx 1$, useful around the shark fins) and in the free stream of the kiln; (ii) it preserves the integrity of the burner jet and resolves the recirculation bubble downstream of the burner tip; and (iii) its far-field prediction is in close agreement with that of the two other 'mainstream' closures (standard and Realizable k–ε), which is a strong indication that the solution obtained with SST k–ω is not an outlier.

III.10 Conclusion

This chapter has been devoted to the construction of the numerical framework used to investigate the flow, the combustion and the heat transfer inside an industrial rotary kiln. The Finite Volume Method has been recalled as the discretization technique on which the analysis is built, and the two pieces of software of the ANSYS 2021 R1 suite have been presented: ICEM CFD for the construction of the geometry and the generation of the mesh, and Fluent 21 for the solution of the governing equations.

Chapter IV:
Results, Analysis and Interpretation

Chapter IV: Results, Analysis and Interpretation

IV.1 Introduction

This chapter presents a comprehensive analysis of the numerical results obtained from Computational Fluid Dynamics (CFD) simulations conducted to investigate the influence of shark fin geometrical modifications on heat transfer enhancement inside a rotary kiln. The primary objective of this parametric study is to identify the geometric configuration of shark- fin turbulators that yields the most favorable thermal performance under industrially relevant operating conditions. Three geometrical parameters are systematically varied: the number of fins, the fin depth, and the fin inclination angle. The influence of each parameter is assessed through five key performance indicators: the axial temperature distribution, the local Nusselt number, the temperature contours, the local friction coefficient, and the turbulent kinetic energy (TKE) distribution, as well as velocity streamline patterns. By correlating thermal enhancement with hydraulic penalties, this study provides a multi-objective perspective essential for engineering design in high temperature industrial applications such as cement kilns, rotary calciners, and drying drums. The results are structured in three main sections corresponding to the three geometric parameters under investigation. Each section includes a thermal analysis subsection and a dynamic (hydrodynamic) analysis subsection, allowing a rigorous evaluation of both the heat transfer augmentation mechanisms and the associated pressure drop penalties. The chapter concludes with a comparative synthesis identifying the optimal fin configuration based on the overall thermal-hydraulic performance.

IV.1.1 Numerical Model Validation and Code Verification

Before conducting parametric investigations, it is imperative to establish the credibility of the numerical methodology by comparing simulation predictions against independent experimental or industrial data. The validation exercise reported here employs temperature measurements obtained from the LAFARGE OGGAZ-MASCARA industrial rotary kiln as the reference dataset.

The CFD simulations were carried out using the Shear Stress Transport (SST) k-ω turbulence model within the FLUENT solver environment. The SST k-ω model is particularly well suited for wall-bounded turbulent flows and blending regions between the near-wall sublayer and the free stream, which are characteristic of rotary kiln flow fields. As illustrated in Figure IV.1 below, the axial temperature profile predicted by the SSTk-ω model is in satisfactory agreement with the industrial kiln temperature data across the full 40-metre length of the kiln. Both datasets capture the sharp temperature peak near $x \approx 7$ m associated with the flame zone and the progressive thermal decay toward the kiln outlet. Minor discrepancies observed between the numerical predictions and the measured data are attributable to inherent simplifications in the computational model, including one-dimensional boundary condition assumptions, the neglect of solid-bed interactions, and the uniform inlet velocity profile imposed at the kiln inlet. Despite these limitations, the overall agreement confirms the capability of the SST k-ω model to reproduce the dominant thermal patterns with sufficient fidelity for parametric design studies. The validated model is therefore adopted as the baseline for all subsequent simulations presented in this chapter.

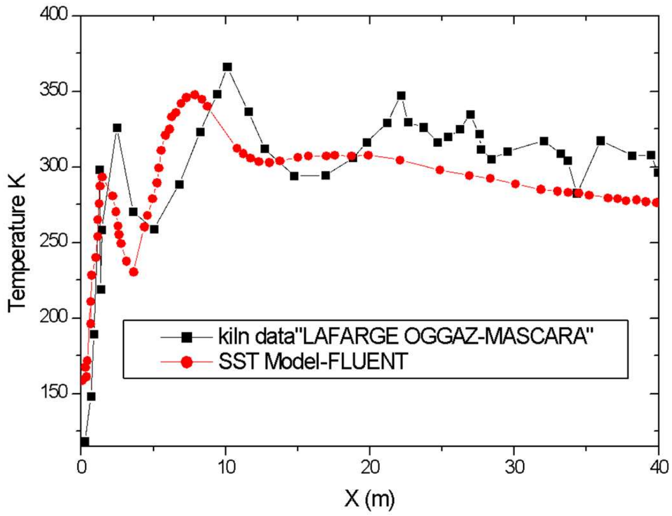

Figure IV.1: Validation and comparison of the SST k-ω turbulence model against industrial kiln temperature data (LAFARGE OGGAZ-MASCARA)

IV.2 Variation of Fin Number

The first parametric investigation examines the influence of the number of shark-fin turbulators mounted on the inner wall of the rotary kiln. Five finned configurations – containing 4, 5, 6, 7, and 8 fins – are compared against a baseline smooth-wall case (Case 1: without fins). The fins are uniformly distributed along the circumference of the kiln, and their depth and angle are held constant throughout this parameter sweep. By isolating the effect of fin multiplicity, this section identifies the threshold at which additional fins continue to provide meaningful thermal gains relative to the hydrodynamic cost incurred.

IV.2.1 Thermal Effect

IV.2.1.1 Impact of Fin Number on Temperature Distribution

Figure 4.2 presents the axial variation of the bulk fluid temperature along the 40-metre kiln length for all six configurations. In the smooth-wall reference case, the temperature profile rises gradually from the inlet, reaches a maximum near the mid-section of the kiln where the heat flux is highest, and thereafter declines toward the outlet due to the progressive reduction of the driving thermal gradient. This relatively flat behavior is a direct consequence of the absence of any active mixing mechanism.

As fins are progressively added from 4 to 8, two mutually reinforcing effects are clearly observable.

First, the amplitude of the temperature oscillations along the kiln axis increases substantially: each fin acts as a local flow obstruction that forces the fluid away from the wall boundary layer, mixes the cooler core flow with the hotter near-wall fluid, and thereby causes sharp local temperature peaks immediately downstream of each fin location. The periodic spacing of the fins along the kiln axis creates a repeating pattern of thermal enhancement zones that sustain elevated temperatures throughout the heated section. Second, the mean bulk temperature at the outlet increases monotonically with fin number. The 8-fin configuration produces the highest outlet temperature among all cases, reflecting the cumulative benefit of increased heat transfer area, stronger recirculation, and more effective disruption of the thermal boundary layer. This result underlines the critical role of fin density in maximizing convective heat extraction from the kiln wall and delivering it to the bulk flow.

From a practical standpoint, the systematic increase in outlet temperature with fin count suggests that an optimal number of fins exists beyond which the additional benefit of adding further fins diminishes while the pressure penalty escalates. This trade-off will be quantified in Section 4.2.2 through the friction coefficient and turbulent kinetic energy analyses.

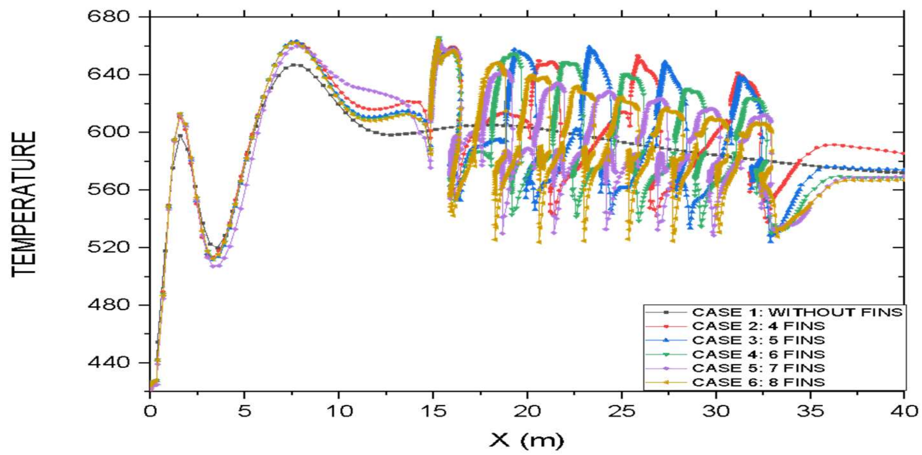

Figure IV.2: Axial temperature variation along the rotary kiln as a function of fin number

IV.2.1.2 Impact of Fin Number on Local Nusselt Number Distribution

Figure IV.3 presents the axial variation of the local Nusselt number Nu along the kiln for all fin configurations. The Nusselt number is a dimensionless measure of the convective heat transfer rate relative to the conductive resistance, and its distribution directly reflects the intensity of thermal boundary-layer disruption along the kiln wall. In the smooth-wall baseline case, the local Nusselt number follows a monotonically decreasing trend from the inlet as the thermal boundary layer develops and thickens, a pattern characteristic of fully developing turbulent pipe flows.

The introduction of fins produces dramatic and highly localized increases in the Nusselt number. Sharp peaks of Nu are observed immediately downstream of each fin, corresponding to regions where the fin-induced recirculation impingement flows attach to the heated wall and locally thin the thermal boundary layer to near-zero thickness. The peak Nusselt number values increase consistently with fin number: the 8-fin configuration (Case 6) yields the highest local Nu values, with peak magnitudes reaching approximately 10,000–12,000 in the central heated section of the kiln. Between the fin peaks, the Nusselt number drops to intermediate values as the reattachment region gives way to a redeveloping boundary layer before the next fin is encountered. The overall average Nusselt number – computed as the length-weighted mean of the local distribution – increases by a factor of approximately 2.5–3 for the 8-fin case compared to the smooth wall, representing a substantial convective enhancement. These findings confirm that shark-fin turbulators are highly effective passive heat transfer augmentation devices whose thermal efficiency scales favorably with fin population density.

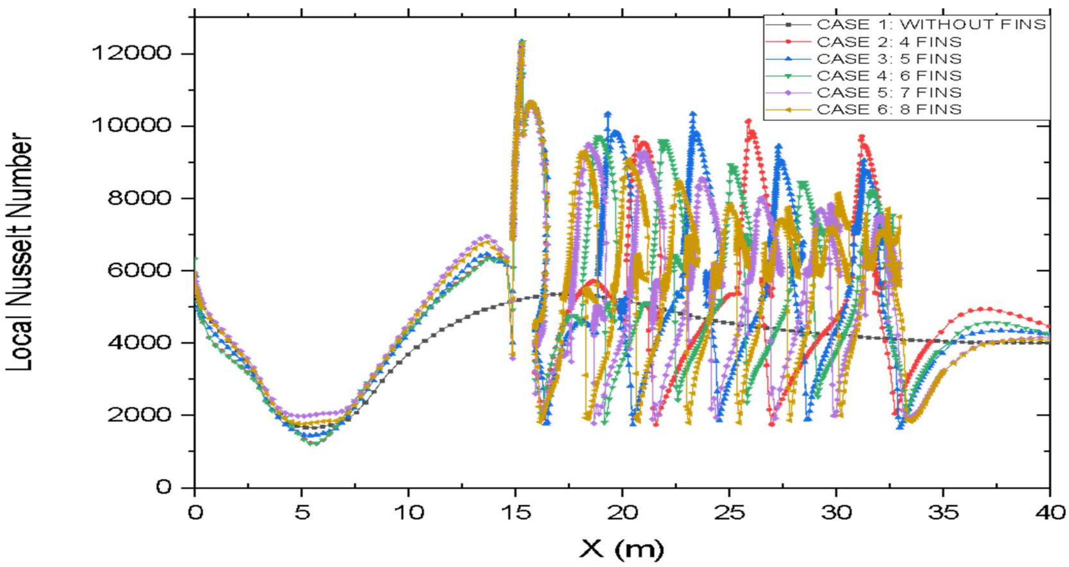

Figure IV.3: Variation of local Nusselt number along the rotary kiln as a function of fin number

IV.2.1.3 Effect of Fin Number on Temperature Contours

Figure IV.4 displays the two-dimensional temperature contour maps on a longitudinal cross-section of the kiln for all configurations, ranging from the smooth-wall case to the 8 fin arrangement. These contour plots provide spatial insight into the three-dimensional heat transfer mechanisms that are necessarily averaged out in the one-dimensional axial profiles of Figures IV.2 and IV.3.

In the smooth-wall case (Case 1), the temperature field exhibits pronounced thermal stratification: the fluid adjacent to the hot kiln wall is maintained at significantly elevated temperatures compared to the cold core, and the thermal gradient decays very slowly along the kiln radius. This indicates that heat is transferred primarily by conduction across a thick boundary layer and that the convective mixing between wall and core regions is minimal. The cold central zone persists over a large fraction of the kiln cross-section, reducing the effective thermal utilisation of the kiln. The progressive addition of fins (4, 5, 6, 7, 8) has a dramatic homogenizing effect on the temperature field. As fin number increases, the cold central zones are systematically eliminated, and the temperature distribution becomes increasingly uniform across the kiln cross-section. For the 8-fin configuration, the temperature contours show near-complete mixing: the distinction between the hot wall region and the cold core has almost disappeared, and the fluid bulk temperature is close to the wall temperature throughout the heated section. This homogenization is a direct consequence of the enhanced secondary flows and vortical structures generated by the fins, which continuously transport hot fluid from the wall into the core and cold fluid from the core toward the wall. The thermal penetration depth – measured as the radial distance over which the temperature decreases from the wall value to within 10% of the core value – increases significantly with fin number, confirming the improved convective mixing efficiency.

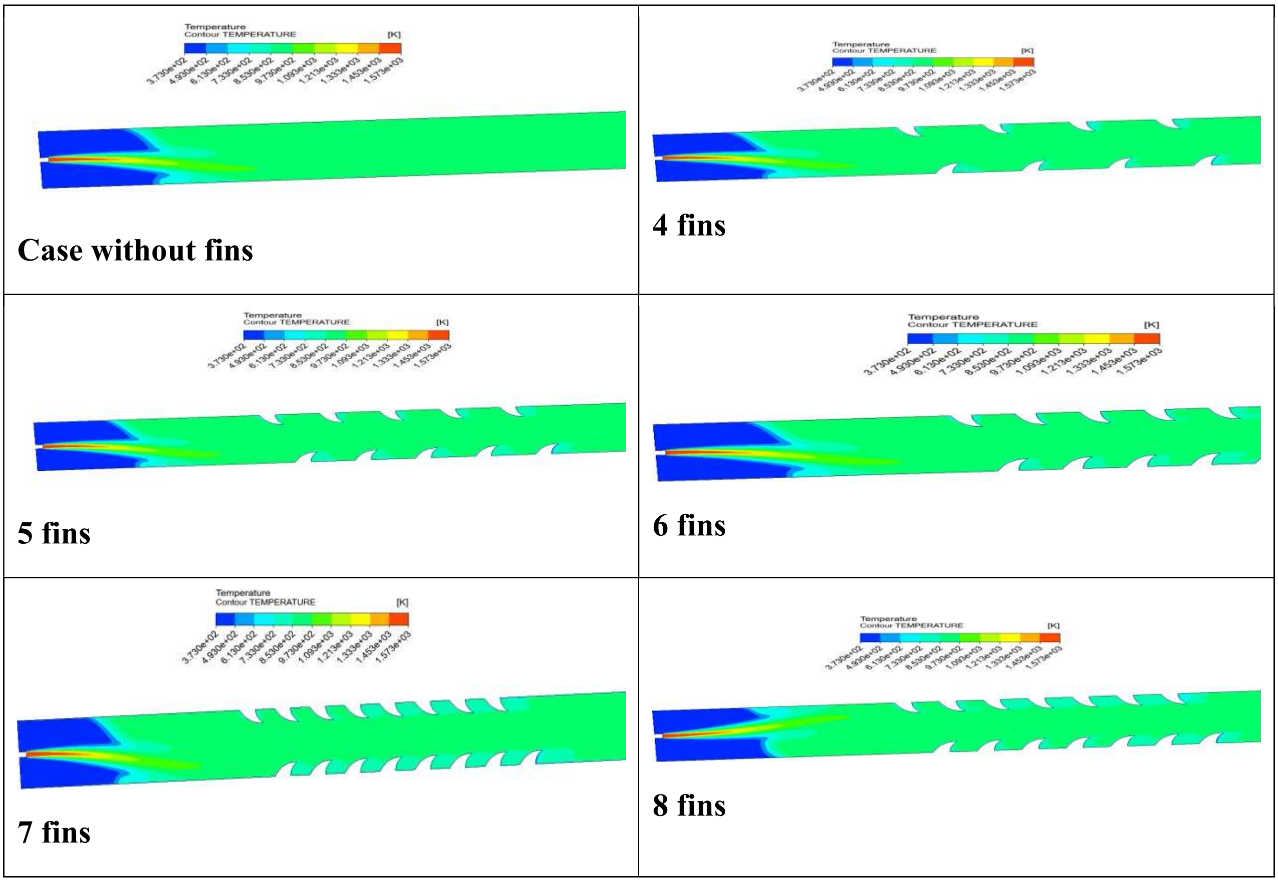

Figure IV.4: Temperature contours along the rotary kiln for varying fin number

IV.2.2 Dynamic (Hydrodynamic) Effect

IV.2.2.1 Effect of Fin Number on Local Friction Coefficient

Figure IV.5 shows the axial distribution of the local friction coefficient Cf along the kiln wall for all fin number cases. The friction coefficient is a direct measure of the wall shear stress and therefore quantifies the hydraulic penalty – i.e., the additional pumping power required to maintain the flow – that accompanies the heat transfer enhancement induced by the fins. In the smooth-wall case, the friction coefficient is very low and nearly constant along the kiln, consistent with the expected behavior of a fully turbulent pipe flow in the absence of geometric perturbations.

As the number of fins increases from 4 to 8, the friction coefficient exhibits periodic, high-amplitude spikes at each fin location. The peaks reflect the localized momentum deficit created by the fin-induced flow separation and reattachment, which dissipate mechanical energy and impose a resistance on the flow. The magnitude of these friction peaks increases monotonically with fin number: the 8-fin configuration generates the highest friction peaks, with Cf values approximately one order of magnitude greater than the smooth-wall baseline at the fin locations. This result highlights the fundamental engineering trade-off inherent in passive heat transfer enhancement: the same geometric features (fins) that generate the recirculation responsible for Nusselt number augmentation are also the source of elevated pressure losses. In a practical kiln design, this trade-off must be evaluated using the thermohydraulic performance factor (PEC), which weighs the Nusselt number improvement against the friction coefficient penalty, to identify the net energy benefit of the enhanced configuration.

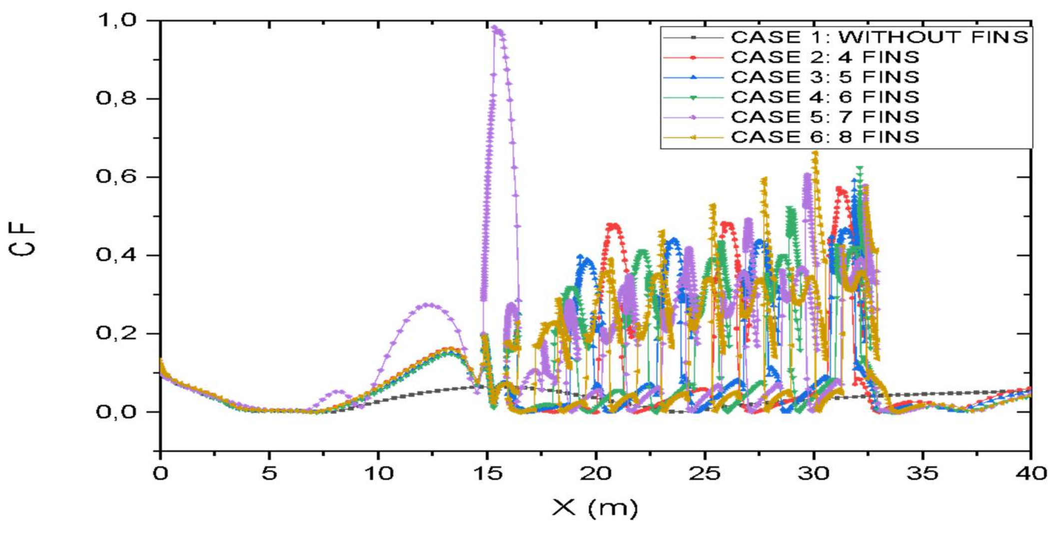

Figure IV.5: Local friction coefficient distribution along the rotary kiln for varying fin number

IV.2.2.2 Effect of Fin Number on Turbulent Kinetic Energy

Figure IV.6 presents the axial variation of the turbulent kinetic energy (TKE) along the kiln centreline for all six fin configurations. TKE is a quantitative measure of the intensity of velocity fluctuations in the turbulent flow field, and its distribution provides direct evidence of the strength of the vortical and recirculation structures generated by the fins. In the smooth-wall baseline, TKE levels are uniformly low throughout the kiln, reflecting the relatively weak turbulence intensity characteristic of a plain pipe flow at the operating Reynolds number.

With the introduction of fins, TKE levels increase dramatically and exhibit sharp, localised peaks at each fin position. These peaks correspond to the separated shear layers that form on the downstream face of each fin and subsequently roll up into coherent vortices. As the number of fins increases from 4 to 8, two trends are clearly visible: the peak TKE values at each fin location increase, and the spatial coverage of elevated TKE extends over a larger fraction of the kiln length. The 8-fin configuration produces the highest and most uniformly distributed TKE levels, indicating that it generates the most vigorous turbulent mixing throughout the kiln. This enhanced turbulence intensity is entirely consistent with the superior Nusselt numbers and temperature homogenization observed for the 8-fin case. The TKE distribution thus provides a mechanistic explanation for the heat transfer improvement: fins generate organized turbulence structures that continuously destroy the laminar sublayer, thin the thermal boundary layer, and promote radial transport of heat from the wall to the bulk flow.

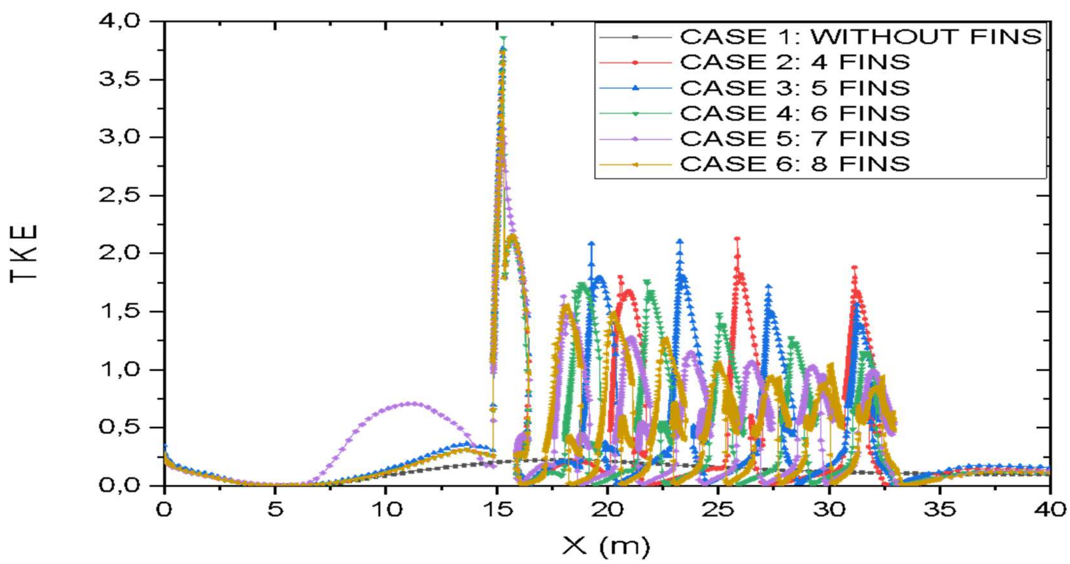

Figure IV.6: Turbulent kinetic energy variation along the rotary kiln: influence of fin number

IV.2.2.3 Effect of Fin Number on Velocity Streamlines

Figures IV.7 present the velocity streamline patterns for all six fin configurations, visualizing the complex secondary flow structures induced by the shark-fin geometry. The streamlines are colored according to local velocity magnitude, ranging from zero at the wall to the maximum core velocity. In the smooth-wall case, the streamlines are nearly parallel to the kiln axis and exhibit a simple parabolic-like velocity profile, confirming the dominance of axial flow with negligible secondary motion.

The introduction of even 4 fins (Case 2) causes a striking transformation of the flow topology. Immediately downstream of each fin, a pair of counter-rotating recirculation vortices forms and occupies a substantial portion of the kiln cross-section. These recirculation zones are responsible for the high Nusselt numbers and TKE peaks observed in the thermal analysis, as they continuously entrain hot near-wall fluid into the cold core. As the fin count increases to 5, 6, 7, and 8, the recirculation zones become more numerous, more intense, and more closely spaced, reducing the effective hydraulic diameter of the undisturbed flow channel and increasing the interaction length between adjacent fin-induced vortices. For the 8-fin configuration, the streamlines reveal a highly complex three-dimensional flow field in which distinct recirculation structures from adjacent fins partially overlap, creating a quasi-continuous zone of turbulent mixing along the entire kiln length. This continuous mixing mechanism is the primary driver of the superior thermal performance observed for the high-fin-count configurations. The progressive evolution of the streamline patterns with increasing fin number provides clear visual confirmation of the heat transfer enhancement mechanism and supports the interpretation of the quantitative Nusselt and TKE results presented in the preceding sub-sections.

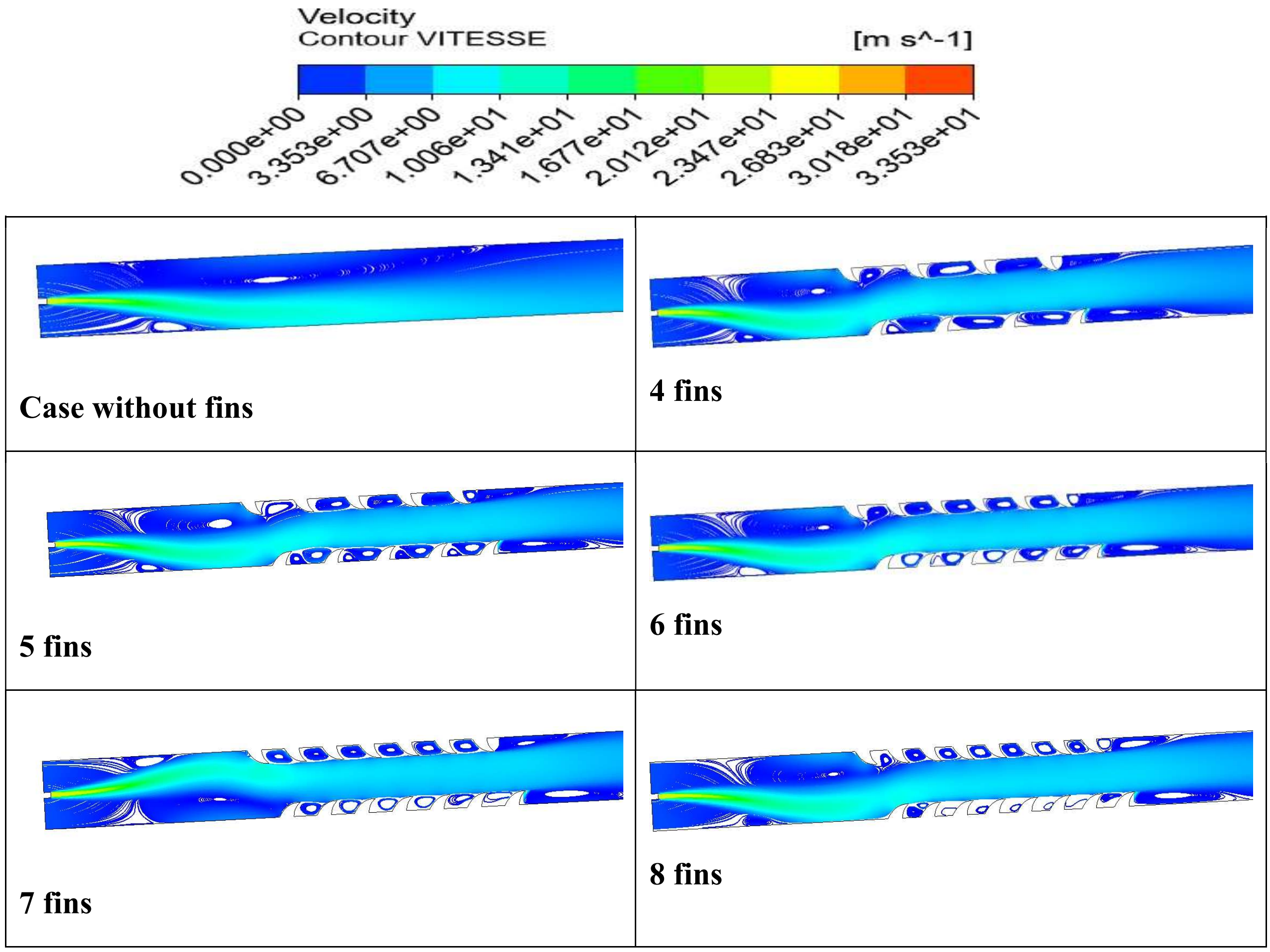

Figure IV.7: Velocity streamlines along the rotary kiln for varying fin number

IV.3 Variation of Fin Depth

The second parametric investigation focuses on the influence of the fin depth-to-hydraulic-diameter ratio Dp (where Dp = h,dh, h being the fin height and dh the hydraulic diameter of the kiln). Four depth values are studied: Dp = 0.25, 0.50, 1.25, and 1.50. The number of fins and their inclination angle are held constant in this sweep. Increasing the fin depth extends the fin surface further into the flow domain, thereby increasing its interaction with the mainstream flow and generating stronger secondary flow structures. This section quantifies the thermal gain and hydraulic penalty associated with progressively deeper fins.

IV.3.1 Thermal Effect

IV.3.1.1 Impact of Fin Depth on Temperature Distribution

Figure IV.8 shows the axial temperature distribution along the kiln for the four fin depth cases. The temperature profile for the shallowest fin (Dp = 0.25) is only marginally superior to the smooth-wall baseline, reflecting the limited interaction between a shallow fin and the bulk flow. As Dp increases to 0.50, a moderate improvement in the outlet temperature is observed, accompanied by more pronounced oscillatory behavior along the kiln axis. This oscillatory pattern is the thermal signature of the flow reattachment process downstream of each fin and its associated localised convective heat transfer peak.

For the deepest fin configurations (Dp = 1.25 and Dp = 1.50), the temperature enhancement is substantial and clearly evident throughout the kiln length. The deepest fin (Dp = 1.50) achieves the highest outlet temperature among all four cases, exceeding the Dp = 0.25 baseline by a significant margin. The mechanism responsible for this improvement is the deeper penetration of the fin into the flow domain: a deeper fin forces a larger volume fraction of the mainstream flow to detour around and over the fin obstruction, creating stronger recirculation zones, greater boundary layer disruption, and more effective radial heat transport. The monotonic increase in mean fluid temperature with fin depth confirms that thermal performance scales favorably with this geometric parameter within the studied range. However, as will be demonstrated in Section 4.3.2, the hydraulic penalty also increases significantly with fin depth, necessitating a balanced evaluation of the optimal depth for a given application.

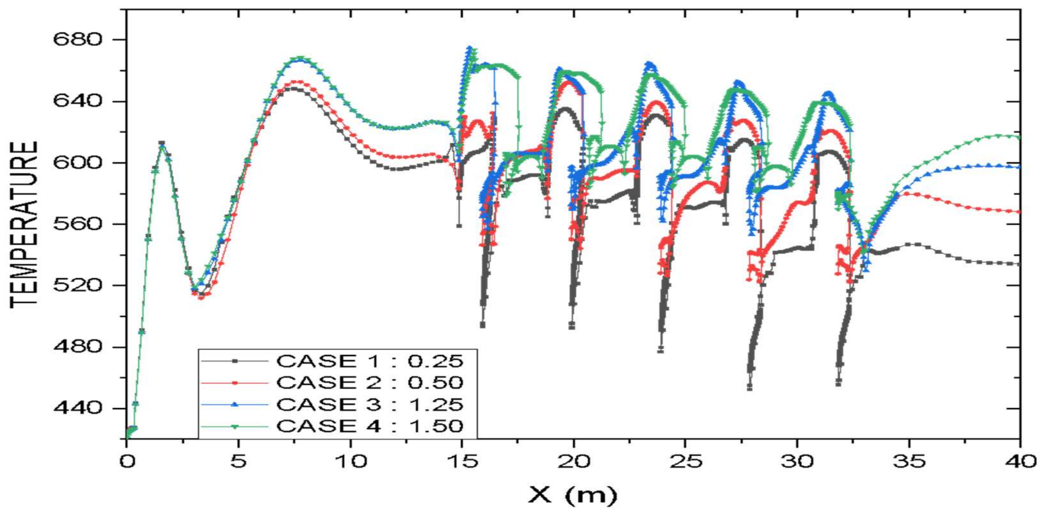

Figure IV.8: Axial temperature variation along the rotary kiln as a function of fin depth

IV.3.1.2 Impact of Fin Depth on Local Nusselt Number Distribution

Figure IV.9 presents the local Nusselt number distribution as a function of fin depth. The deepest fin configuration (Dp = 1.50, Case 4) yields the highest Nusselt number values throughout the kiln, with peak values reaching approximately 14,000–17,000 in the central heated zone, representing a near three-fold increase over the shallowest fin case. The Nusselt number enhancement mechanism is directly linked to the fin depth: a deeper fin creates a more intense separated shear layer on its downstream face, generates a larger recirculation zone with higher turbulent kinetic energy, and produces a more vigorous impingement of the reattachment flow on the heated kiln wall downstream of the fin location. The local Nusselt number peaks associated with the fin locations shift slightly in both magnitude and axial position as Dp increases, reflecting changes in the reattachment length scale. For shallow fins, the reattachment point is located relatively close to the fin base, producing a compact but intense heat transfer peak. For deeper fins, the reattachment point moves further downstream, spreading the heat transfer enhancement over a slightly larger axial distance and producing a broader, higher Nusselt peak. This spatial redistribution of the heat transfer enhancement has practical implications for the design of kiln heating profiles, as it influences the distribution of thermal energy input along the kiln length.

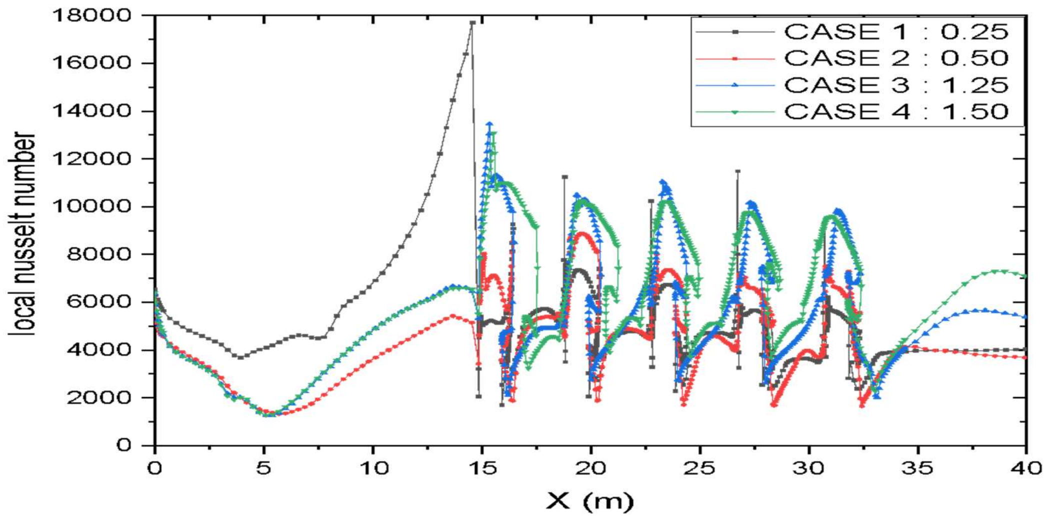

Figure IV.9: Variation of local Nusselt number along the rotary kiln as a function of fin depth

IV.3.1.3 Effect of Fin Depth on Temperature Contours

Figure IV.10 displays the temperature contour maps for all four fin depth cases. The shallow fin (Dp = 0.25) produces a temperature field that resembles the smooth-wall case in terms of boundary-layer structure, with a persistent cold core and relatively limited thermal penetration into the bulk flow. The transition from Dp = 0.25 to Dp = 0.50 produces a noticeable improvement in temperature uniformity, with the cold central zone contracting in size, particularly in the downstream half of the kiln.

For the deeper fins (Dp = 1.25 and 1.50), the temperature field undergoes a qualitative transformation. The radial temperature gradient is dramatically reduced, and the cross-sectional temperature distribution becomes nearly homogeneous even in the upstream portion of the kiln. Thermal energy penetrates to the kiln centreline at much earlier axial locations compared to the shallower fin cases, indicating a fundamentally different heat transfer mechanism driven by large-scale radial mixing rather than diffusion-dominated boundary-layer conduction. The spatial extent of the high-temperature zone (represented by yellow and green contours) expands significantly with increasing fin depth, confirming the progressive improvement in thermal performance. These contour results are entirely consistent with the quantitative Nusselt number data presented in Figure IV.9 and provide the spatial context needed to understand the flow physics underlying those heat transfer trends.

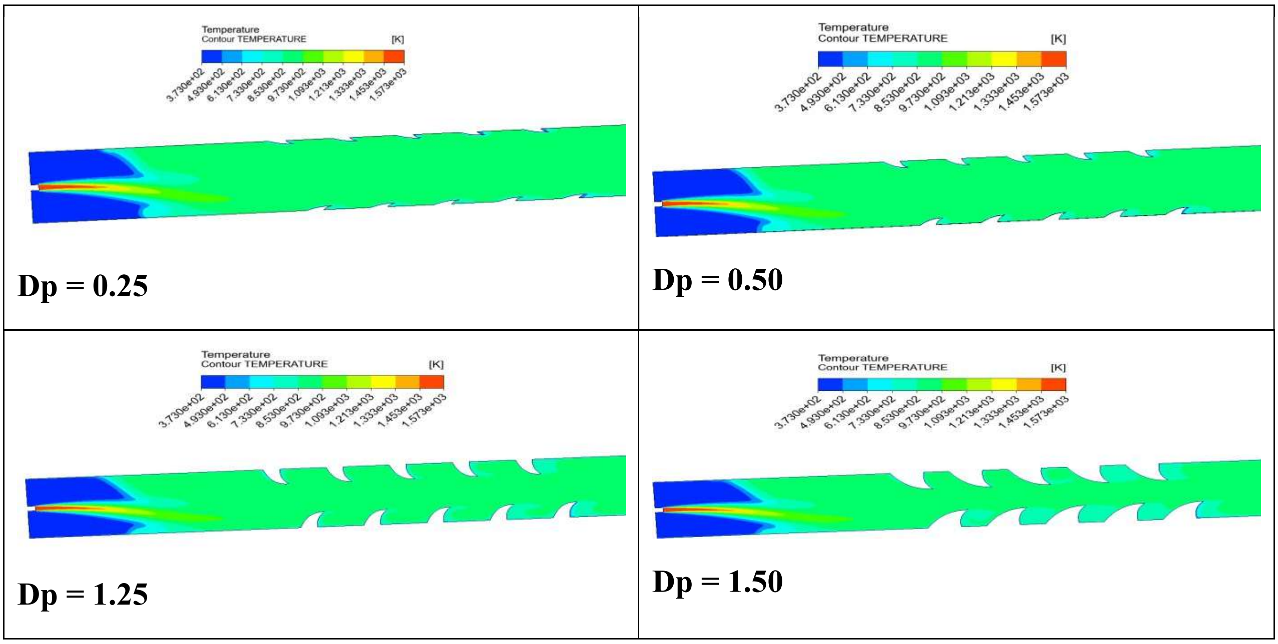

Figure IV.10: Temperature contours along the rotary kiln for varying fin depth

IV.3.2 Dynamic (Hydrodynamic) Effect

IV.3.2.1 Effect of Fin Depth on Local Friction Coefficient

Figure IV.11 shows the local friction coefficient distribution for the four fin depth cases. As anticipated, the friction coefficient increases monotonically with fin depth. The shallowest fin (Dp = 0.25) produces only a modest friction penalty, with peak Cf values slightly above the smooth-wall level. In contrast, the deepest fin (Dp = 1.50) generates much higher Cf peaks at each fin location, reaching values of 0.6–0.7 in the central heated zone compared to near-zero values in the smooth-wall case.

The physical mechanism responsible for this increase is the larger flow blockage ratio associated with deeper fins: a fin with Dp = 1.50 occupies a significantly larger fraction of the flow cross-section than a fin with Dp = 0.25, forcing a greater deflection of the mainstream flow and creating a stronger adverse pressure gradient in the recirculation zone behind the fin. This adverse pressure gradient drives more severe flow separation, larger recirculation bubbles, and therefore higher viscous dissipation and wall friction. The strong dependence of the friction coefficient on fin depth reinforces the importance of conducting a thermohydraulic optimization study that simultaneously considers both the Nusselt number and friction coefficient trends, rather than selecting the deepest fin purely on the basis of thermal performance.

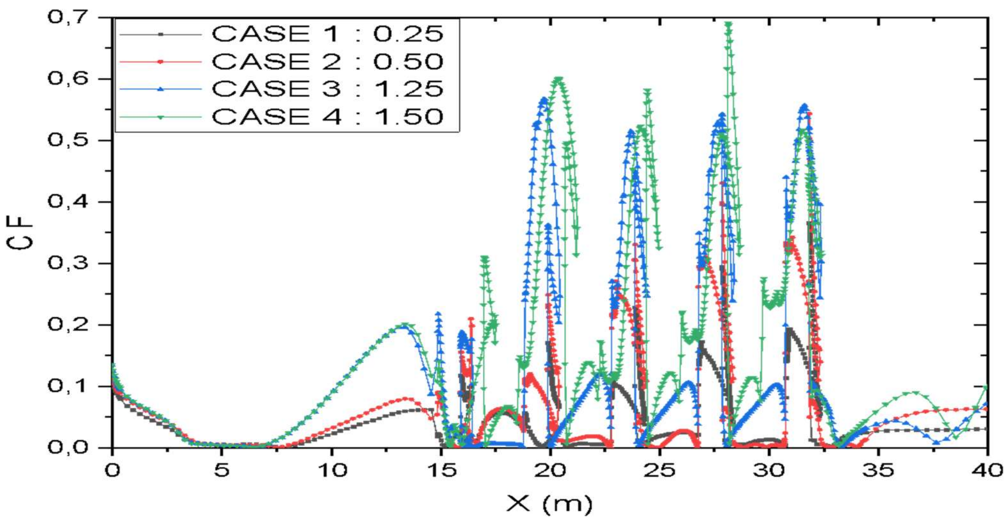

Figure IV.11: Local friction coefficient distribution along the rotary kiln for varying fin depth

IV.3.2.2 Effect of Fin Depth on Turbulent Kinetic Energy

Figure IV.12 illustrates the turbulent kinetic energy distribution for the four fin depth cases. TKE levels increase consistently with fin depth: the shallow fin (Dp = 0.25) produces only modest TKE peaks, while the deepest fin (Dp = 1.50) generates the highest and most spatially extensive turbulence levels along the kiln length, consistent with the larger recirculation zones associated with deeper fin penetration into the flow.

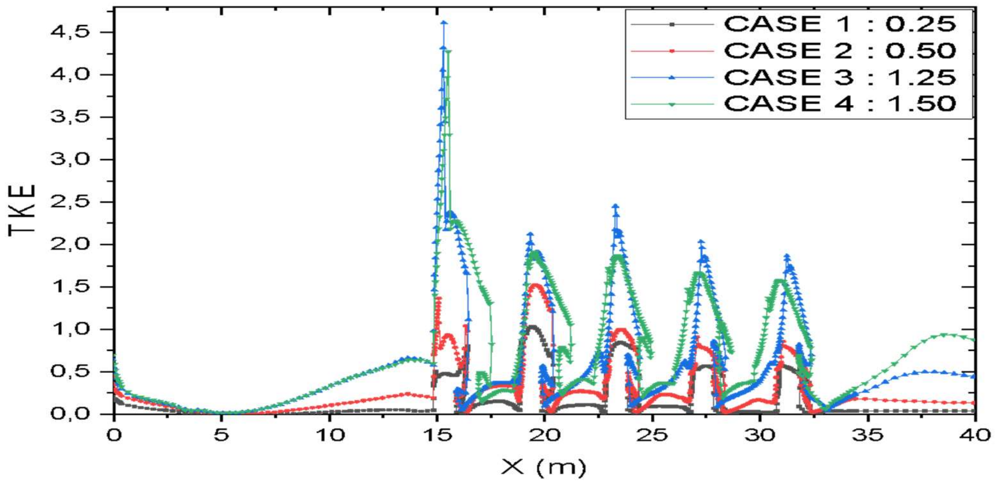

Figure IV.12: Turbulent kinetic energy variation along the rotary kiln: influence of fin depth

IV.3.2.3 Effect of Fin Depth on Velocity Streamlines

Figures IV.13 illustrate the evolution of the velocity streamline topology as a function of fin depth. For the smooth-wall reference (Dp = 0), the streamlines confirm the absence of secondary flow structures, with the flow following smooth parallel paths along the kiln axis. The introduction of a shallow fin (Dp = 0.25) begins to perturb this pattern: small recirculation bubbles appear immediately downstream of the fins, but their spatial extent is limited, and the mainstream flow recovers rapidly. As the fin depth increases to Dp = 0.50, the recirculation bubbles grow noticeably and exhibit stronger rotational velocities, indicating higher TKE levels consistent with Figure 4.12.

For the deepest fins (Dp = 1.25 and 1.50), the streamline patterns reveal substantially larger and more intense vortical structures that occupy a significant fraction of the kiln cross-section. The recirculation zones in the Dp = 1.50 case extend both axially and radially over much greater distances than those in the shallow-fin cases, creating an extended region of intense fluid-wall interaction that is directly responsible for the superior heat transfer observed in the Nusselt number and temperature contour analyses. The strong vortical motion also induces centrifugal effects that enhance the radial transport of both momentum and thermal energy, further contributing to the homogenization of the temperature field. These streamline visualizations provide compelling mechanistic evidence that fin depth is a primary geometric control variable governing the strength and spatial extent of the secondary flow structures responsible for heat transfer enhancement in shark-fin turbulated rotary kilns.

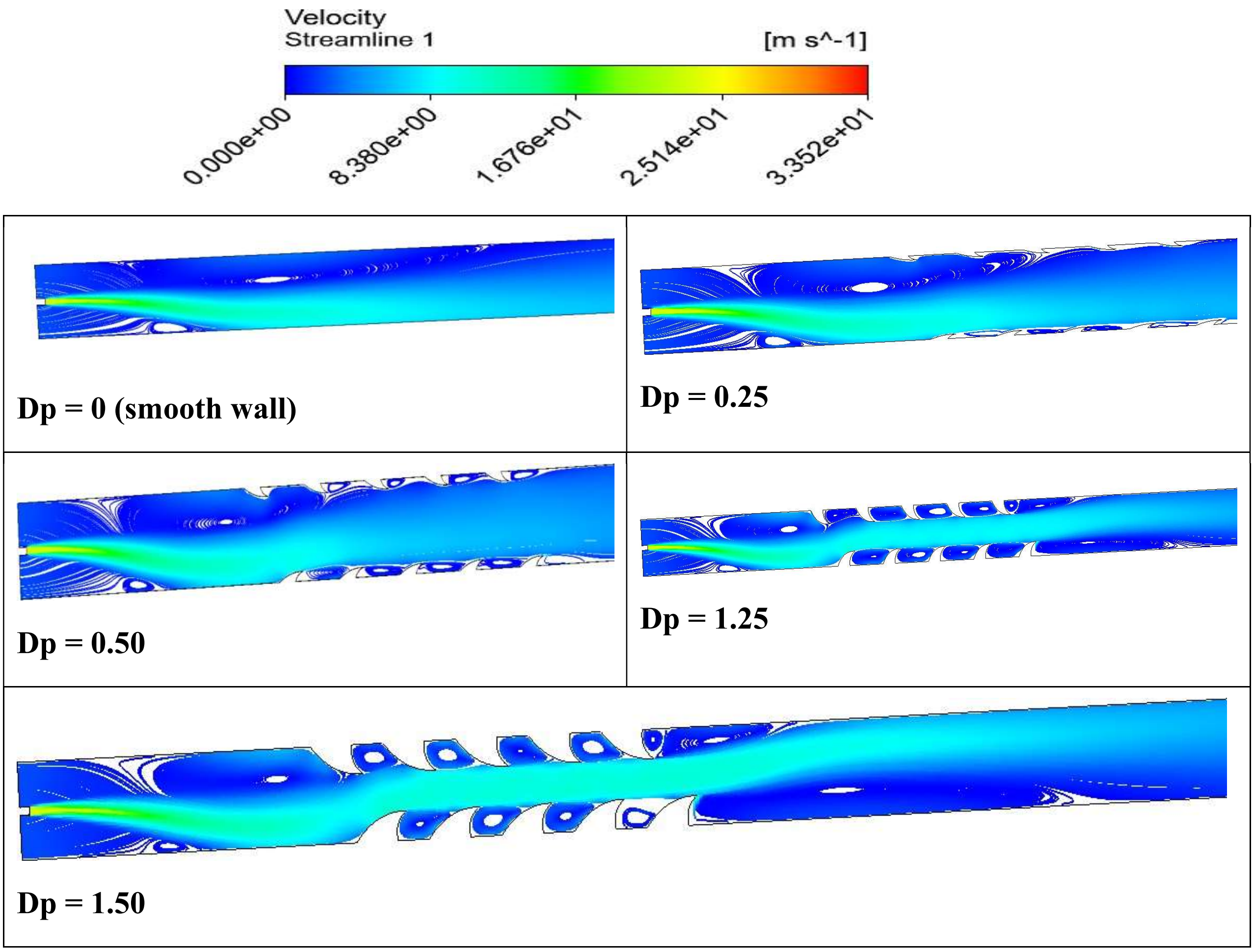

Figure IV.13: Velocity streamlines along the rotary kiln for varying fin depth

IV.4 Variation of Fin Inclination Angle

The third and final parametric investigation examines the effect of the shark-fin inclination angle α on the thermal and hydrodynamic performance of the kiln. Three angle values are studied: α = 30°, 60°, and 90°, where α is measured between the fin face and the kiln axis. The number of fins and their depth are maintained constant across all cases in this parameter sweep. The inclination angle governs the orientation of the flow deflection induced by the fin relative to the main flow direction: a perpendicular fin (α = 90°) maximises the momentum exchange between the fin and the flow, while an oblique fin (α = 30°) provides a gentler deflection. This section quantifies how this geometric variable modulates the thermal performance metrics and the associated hydraulic penalties.

IV.4.1 Thermal Effect

IV.4.1.1 Impact of Fin Angle on Temperature Distribution

Figure IV.14 shows the axial temperature profiles for the three fin angle cases. Among the three configurations studied, the 90° fin (Case 3) achieves the highest fluid temperatures throughout the kiln length, with a particularly notable superiority in the central and downstream sections. The temperature oscillations are most pronounced for this configuration, reflecting the highest heat transfer intensity per unit axial length. The 60° configuration (Case 2) occupies an intermediate position, producing temperature levels that are clearly superior to the 30° case but somewhat below those of the 90° configuration. The 30° fin (Case 1) provides the weakest heat transfer augmentation among the three, with temperature profiles only marginally above those expected for a smooth-wall kiln. This trend can be explained by the angle-dependent flow deflection mechanism: a 90° fin presents its full projected area perpendicular to the incoming flow, maximising both the flow obstruction and the strength of the recirculation zone, while the 30° fin presents a much smaller effective cross-sectional area to the flow, reducing the deflection angle and consequently weakening the secondary flow structures.

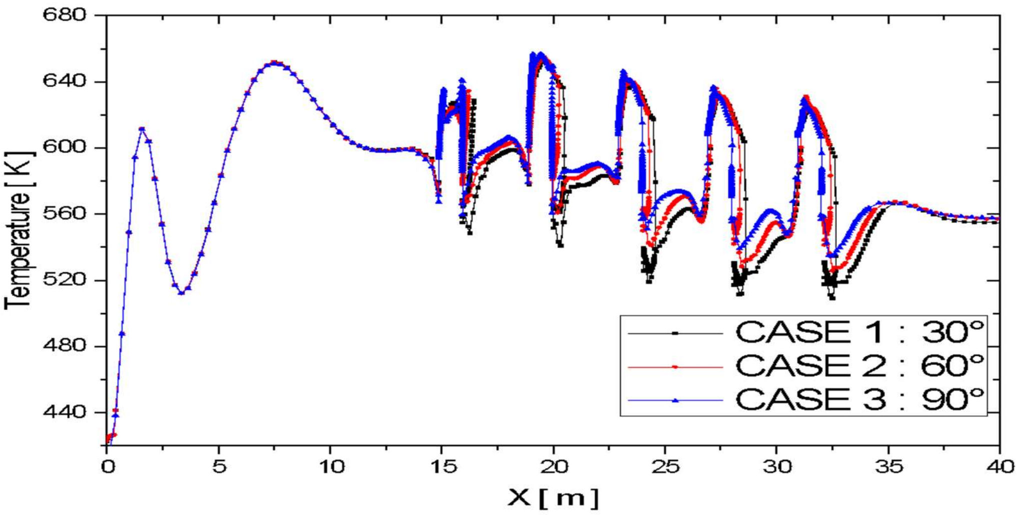

Figure IV.14: Axial temperature variation along the rotary kiln as a function of fin inclination angle

IV.4.1.2 Impact of Fin Angle on Local Nusselt Number Distribution

Figure IV.15presents the local Nusselt number distributions for the three fin angle cases. Consistent with the temperature analysis, the 90° fin configuration produces the highest local Nusselt numbers, with peak values approximately 1.5 times greater than those of the 30° case at the same fin locations. The Nusselt number profiles for all three cases exhibit the characteristic periodic peak structure associated with the fin-induced reattachment zones, but the magnitude of these peaks differs substantially between configurations.

The angle dependence of the Nusselt number can be rationalized through the impingement heat transfer mechanism. A 90° fin deflects the approaching flow almost perpendicularly to the kiln wall, creating a strong impingement jet that strikes the heated wall downstream of the fin with high momentum. This impingement jet thins the thermal boundary layer to a minimum, maximizes the convective heat transfer coefficient, and produces the sharp, high-magnitude Nusselt peaks observed in Figure IV.15.

For the 30° fin, the flow deflection is primarily streamwise rather than wall-normal, resulting in a weaker impingement effect and consequently lower Nusselt peak values. The 60° configuration represents an intermediate case in which the flow deflection has both a significant wall-normal and a streamwise component, explaining its intermediate Nusselt performance. These findings highlight the critical role of fin inclination angle in controlling the direction and intensity of the impingement heat transfer mechanism.

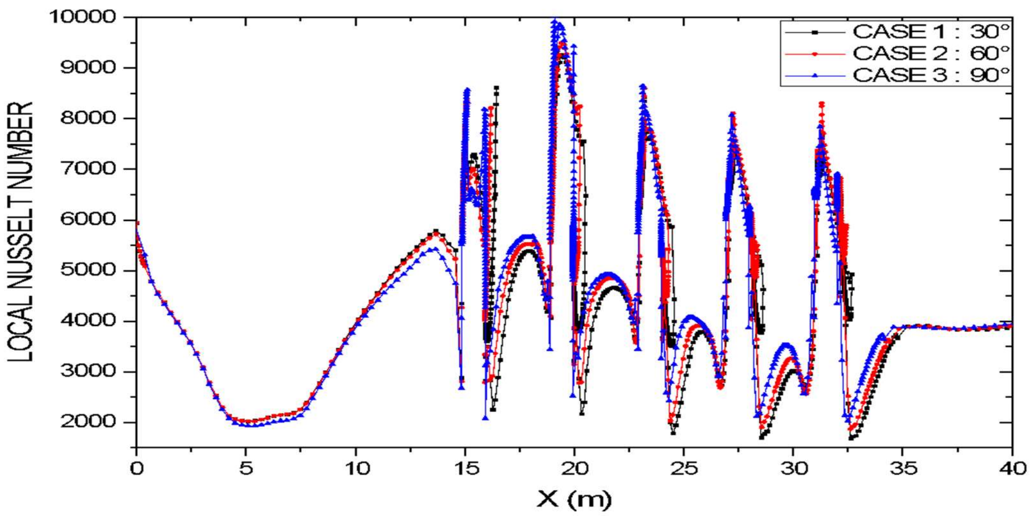

Figure IV.15: Variation of local Nusselt number along the rotary kiln as a function of fin inclination angle

IV.4.1.3 Effect of Fin Angle on Temperature Contours

Figure IV.16 displays the temperature contour maps for the 30°, 60°, and 90° fin configurations. The evolution of the temperature field with increasing fin angle reinforces the quantitative trends identified in the axial profiles and Nusselt distributions. For the 30° case, the temperature field retains significant radial stratification: a distinct cold core region persists along the kiln centreline, and the thermal gradient between the wall and the core is steep throughout the kiln length. This indicates that the oblique fin geometry provides insufficient radial mixing to overcome the natural stratification of the thermal boundary layer.

As the fin angle increases to 60°, the cold core region diminishes in size, and the cross-sectional temperature distribution becomes more uniform. The improvement is particularly evident in the central heated section of the kiln, where the more effective flow deflection of the 60° fin begins to transport thermal energy to the kiln centreline. For the 90° perpendicular fin (Case 3), the temperature contours reveal the most homogeneous cross-sectional distribution among the three configurations: the radial temperature gradient is minimal, the cold core has virtually disappeared, and the bulk fluid temperature is close to the wall temperature throughout the heated section. This near-complete thermal homogenisation at 90° is a direct consequence of the strong wall-normal impingement flows generated by perpendicular fins, which create intense radial heat transport and eliminate the thermal stratification that limits performance in the lower-angle cases. The 90° configuration therefore represents the optimal inclination angle for maximising convective heat transfer in this parametric study.

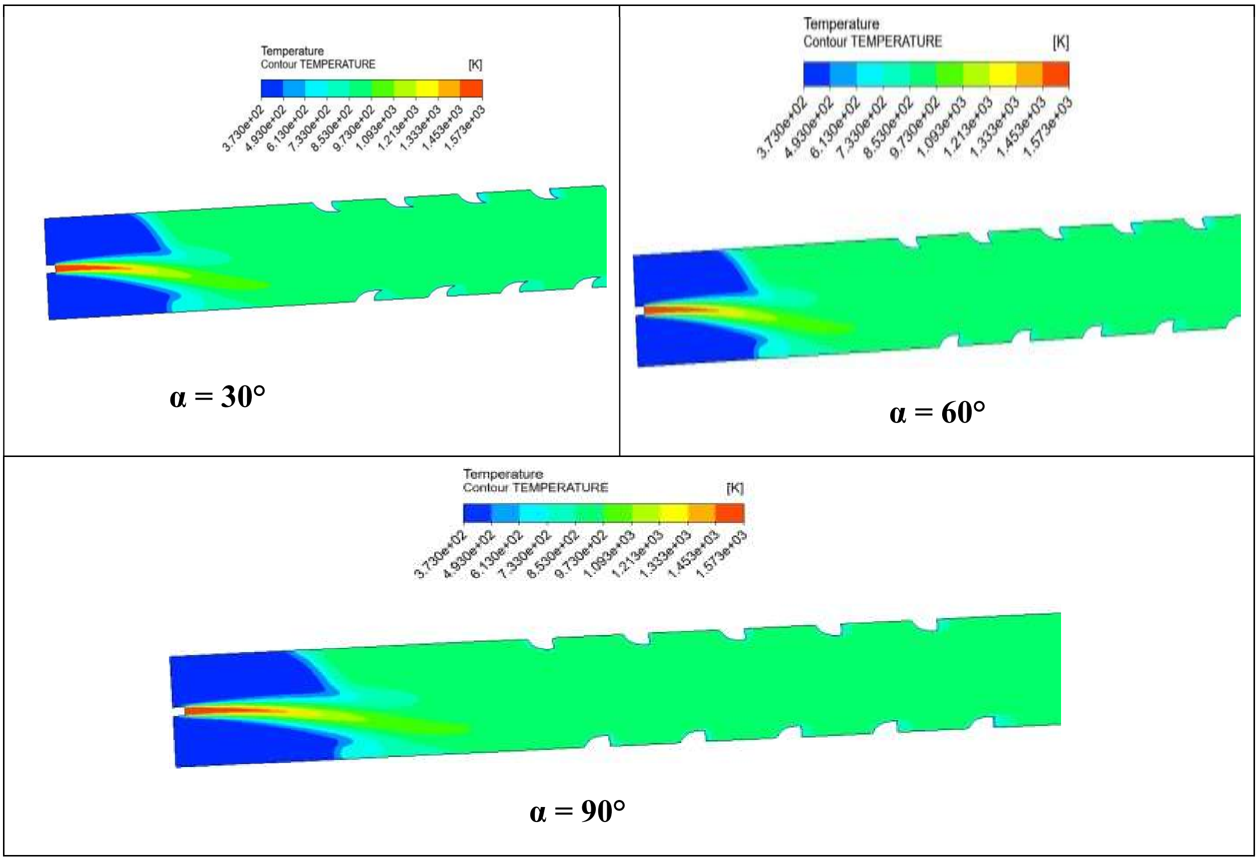

Figure IV.16: Temperature contours along the rotary kiln for varying fin inclination angle

IV.4.2 Dynamic (Hydrodynamic) Effect

IV.4.2.1 Effect of Fin Angle on Local Friction Coefficient

Figure IV.17 illustrates the effect of fin inclination angle on the local friction coefficient distribution. A clear and consistent trend is observed: the friction coefficient increases with fin angle, with the 90° configuration producing the highest friction penalty and the 30° configuration yielding the lowest. The physical basis for this trend is the projected frontal area of the fin perpendicular to the flow: a 90° fin presents its maximum frontal area to the incoming flow, creating the strongest adverse pressure gradient and the most severe flow separation. The resulting recirculation zone is both larger and more energetic than those produced by lower-angle fins, leading to higher viscous dissipation and wall shear stress. The 30° fin, in contrast, presents a minimal frontal area to the flow and produces relatively mild flow separation, with correspondingly lower friction penalties.

The friction coefficient peaks for the 90° case are approximately 2–3 times higher than those for the 30° case at the same fin locations, indicating that the hydraulic penalty is strongly sensitive to fin angle. This result has important practical implications: while the 90° fin provides superior heat transfer performance, it also imposes the highest-pressure loss, and the net energy benefit of this configuration must be evaluated against the increased pumping power requirement. In industrial rotary kilns where energy efficiency is a primary design criterion, the selection of fin angle must therefore account for both the Nusselt gain and the friction penalty to identify the configuration that maximizes the thermohydraulic performance factor.

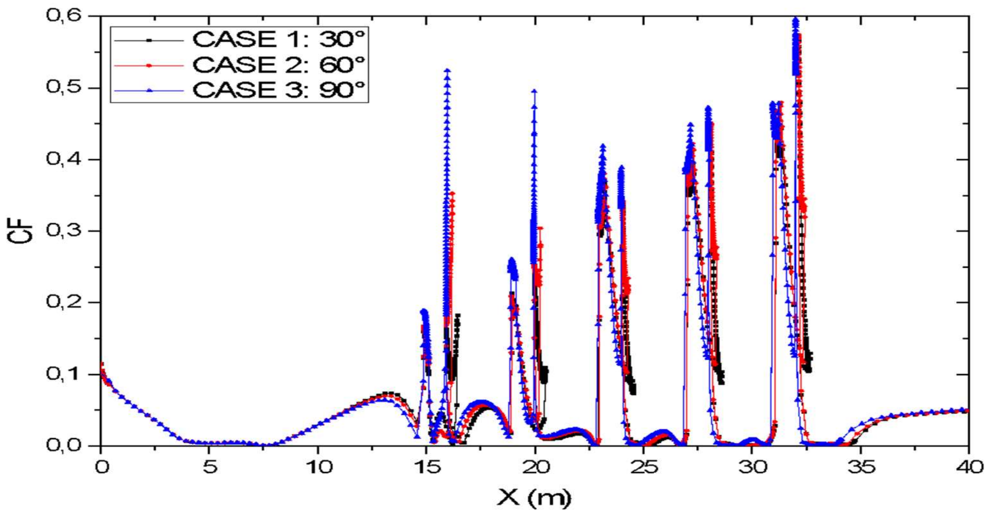

Figure IV.17: Local friction coefficient distribution along the rotary kiln for varying fin inclination angle

IV.4.2.2 Effect of Fin Angle on Turbulent Kinetic Energy

Figure IV.18 shows the TKE distributions for the three fin angle cases. The 90° configuration generates the highest TKE levels, with peak values that substantially exceed those of the 60° and 30° cases at each fin location. As with the previous parametric studies, this TKE enhancement is mechanistically linked to the heat transfer improvement through the boundary-layer disruption mechanism: higher TKE implies stronger velocity fluctuations, a thinner viscous sublayer, and more vigorous turbulent diffusion of thermal energy from the wall to the bulk flow. The 30° fin produces the weakest TKE signature, confirming the limited turbulence generation capacity of oblique fin geometries. The intermediate 60° case produces TKE levels and spatial distributions that are closely aligned with those of the 90° case in the upstream section of the kiln but diverge progressively toward the outlet, suggesting that the 90° fin is more effective at sustaining turbulence over extended kiln lengths. This sustained turbulence production is particularly valuable in long rotary kilns where maintaining effective heat transfer over the full kiln length is essential for achieving the desired material processing temperature.

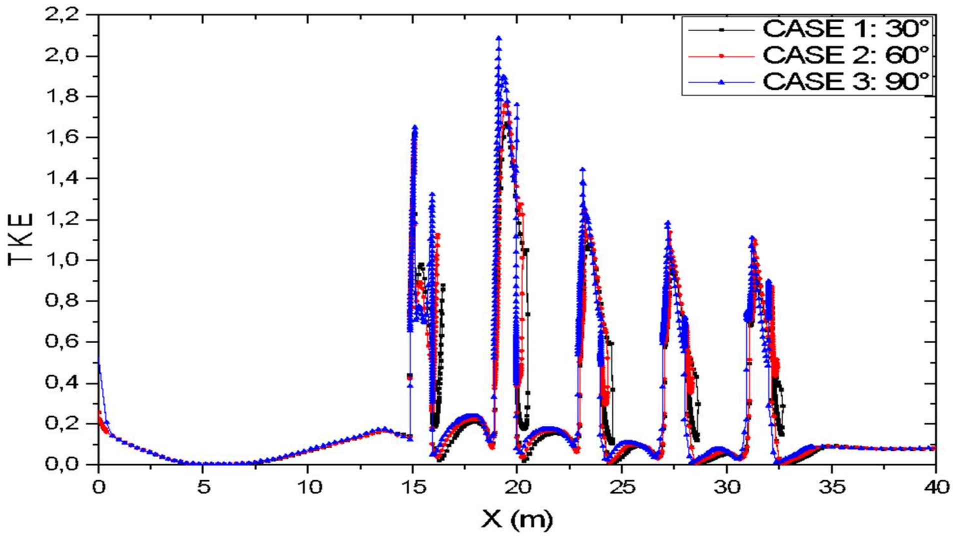

Figure IV.18: Turbulent kinetic energy variation along the rotary kiln: influence of fin inclination angle

IV.4.2.3 Effect of Fin Angle on Velocity Streamlines

Figure IV.19 presents the velocity streamline patterns for the three fin angle configurations. The streamline visualisations provide a comprehensive picture of the three-dimensional flow topology modifications induced by the fin inclination angle and offer a direct mechanistic explanation for the thermal and friction coefficient trends discussed in the preceding sub-sections. For the 30° fin configuration, the streamlines show relatively modest deflection from the axial direction, with small recirculation bubbles forming immediately downstream of each fin. The secondary flows are predominantly aligned with the streamwise direction, and the wall-normal velocity component is limited, explaining the weak impingement heat transfer observed in the Nusselt profiles. As the angle increases to 60°, the streamlines reveal substantially larger and more energetic recirculation zones. The flow deflection now has a significant wall-normal component, and the reattachment region downstream of each fin is characterised by high-velocity fluid impinging on the kiln wall at a moderate angle. For the 90° perpendicular fin, the streamline pattern is qualitatively different from both lower-angle cases: the flow encounters the fin as a nearly blunt obstacle, is forced to separate at the fin edges, and forms a large, symmetric recirculation zone directly behind the fin. The reattachment flow strikes the downstream kiln wall at a near-normal angle, creating the strongest possible impingement heat transfer.

The progressive intensification of the recirculation structures with increasing fin angle, clearly visible in the streamline visualisations, provides the physical justification for the observed monotonic increase in Nusselt number, friction coefficient, and TKE from α = 30° to α = 90°.

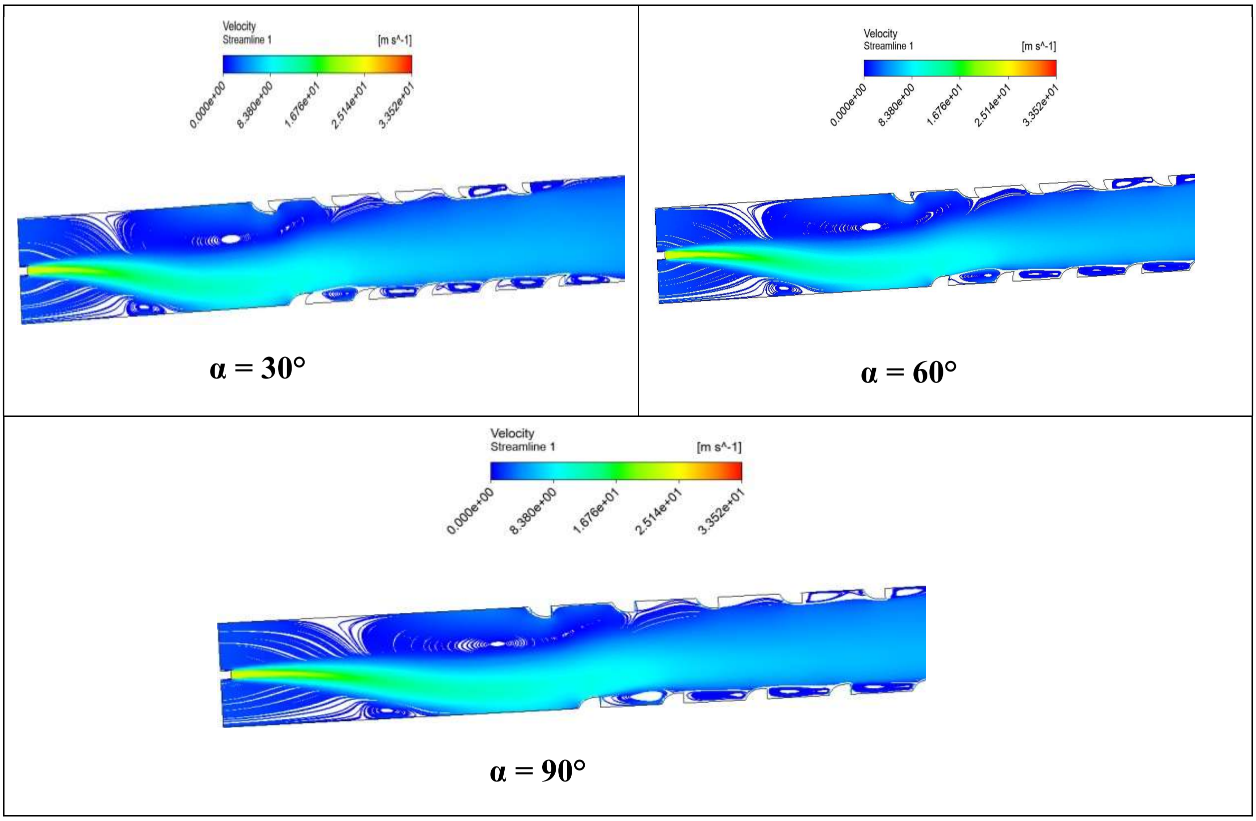

Figure IV.19: Velocity streamlines along the rotary kiln for varying fin inclination angle

IV.5 Conclusion

This chapter presents a detailed numerical analysis of the effect of shark-fin fin geometric parameters on the thermal and hydrodynamic behavior of a rotary kiln. The CFD results show that the presence of the fins significantly improves heat transfer compared to the reference case without fins. This improvement is primarily due to the generation of turbulent structures, the disruption of the thermal boundary layer, and increased radial mixing. The study of the number of fins shows that increasing the number of fins improves heat transfer but also increases pressure drop. An intermediate configuration therefore offers a better compromise. Analysis of fin depth indicates that excessive depth creates high hydraulic resistance. A depth ratio of Dp = 0.5 achieves sufficient thermal improvement with a limited energy penalty. Regarding the inclination angle, an angle of α = 30° yields the best overall performance by effectively disrupting the flow while maintaining a low friction coefficient. Thus, the optimal combination identified in this study is

5 fins; Dp = 0.5; α = 30°. This configuration represents the best compromise between heat transfer enhancement and energy efficiency.

General Conclusion

This thesis investigated the potential of improving heat transfer in cement rotary kilns through the use of internal fins by means of Computational Fluid Dynamics (CFD). The work combined a detailed review of rotary kiln heat-transfer mechanisms with the development of A Two-dimensional numerical model capable of predicting the coupled effects of turbulence, convection, conduction, and thermal radiation. The numerical methodology was established using the Finite Volume Method implemented in ANSYS ICEM CFD and ANSYS Fluent, and its reliability was supported through mesh-independence and turbulence-model assessments.

The parametric study demonstrated that the geometry of the internal fins has a significant influence on the thermal and hydrodynamic behavior of the kiln. Increasing the number of fins enhanced the heat-transfer area and promoted greater thermal uniformity, while variations in fin depth and inclination angle modified the balance between heat-transfer enhancement and flow resistance. The analysis of temperature fields, local Nusselt number, friction coefficient, turbulent kinetic energy, and velocity streamlines showed that appropriately designed fins improve mixing and increase the overall heat-transfer rate. Nevertheless, excessively large or improperly oriented fins may generate higher pressure losses and unnecessary turbulence, reducing the overall efficiency of the system.

Overall, the results confirm that internal fins represent a promising passive technique for enhancing the thermal performance of cement rotary kilns and reducing the energy required for clinker production. The proposed CFD framework provides an effective tool for evaluating and optimizing internal heat-transfer enhancement devices before industrial implementation. Future work should include experimental validation, transient simulations, conjugate heat-transfer analysis, particle-scale modeling using CFD–DEM coupling, chemical reaction kinetics, refractory degradation, and optimization algorithms to identify the most efficient fin configurations under realistic industrial operating conditions. These developments would further strengthen the applicability of the proposed approach and contribute to more energy-efficient and environmentally sustainable cement manufacturing.

Bibliography

1. Cement and Concrete – Breakthrough Agenda Report ,International Energy Agency, International Energy Agency. 2025.
2. Global Cement and Concrete Association. Concrete Future: The GCCA 2050 Cement and Concrete Industry Roadmap for Net Zero Concrete , Global Cement; Concrete Association. 2021.
3. G. Habert ,Environmental Impacts and Decarbonization Strategies in the Cement and Concrete Industries, Nature Reviews Earth & Environment. 2020. Vol. 1, no. 11. P. 559–573. DOI: 10.1038,s43017-020-0093-3.
4. Barbhuiya S., Das B. B., Adak D. Roadmap to a Net-Zero Carbon Cement Sector: Strategies, Innovations and Policy Imperatives , Journal of Environmental Management. 2024. Vol. 359. P. 121052. DOI: 10.1016,j.jenvman.2024.121052.
5. Mungyeko Bisulandu B.-J. R., Huchet F. Rotary Kiln Process: An Overview of Physical Mechanisms, Models and Applications , Applied Thermal Engineering. 2023. Vol. 221. P. 119637. DOI: 10.1016,j.applthermaleng.2022.119637.
6. I. Qasim ,Heat Loss Quantification and Heat Transfer in Rotary Kilns for Calcination and Clinker Formation: From Combustion and Electrification at 150 kW to Industrial Scale , Industrial & Engineering Chemistry Research. 2025. Vol. 64. P. 11531–11543. DOI: 10.1021,acs. iecr.5c00704.
7. M. C. Siame, Dynamic Simulation of Heat Distribution and Losses in Cement Kilns for Sustainable Energy Consumption in Cement Production, Sustainability. 2025.Vol. 17, no. 2. P. 553. DOI: 10.3390, su17020553.
8. A. Gunnarsson , Discrete-Ordinates Modelling of the Radiative Heat Transfer in a Pilot-Scale Rotary Kiln , Energies. 2020. Vol. 13, no. 9. P. 2192. DOI: 10.3390,en13092192.
9. Witt P. J., Johnson J., Schwarz M. P. An Efficient Method for Computational Flow-Based Simulation of Heat Transfer in a Rotary Kiln with Pilot Scale Validation , Applied Thermal Engineering. 2022. Vol. 214. P. 118894. DOI: 10.1016,j.applthermaleng.2022.118894.
10. Ryan J., Bussmann M., DeMartini N. CFD Modelling of Calcination in a Rotary Lime Kiln , Processes. 2022. Vol. 10, no. 8. P. 1516. DOI: 10.3390,pr10081516.
11. J. L. Svensen, A Dynamical Simulation Model of a Cement Clinker Rotary Kiln,

Proceedings of the 2024 European Control Conference. IEEE, 2024. P. 2162–2168. DOI: 10.23919,ECC64448.2024.10590953.

12. C. Pieper , Numerical Investigation of the Impact of Coating Layers on RDF Combustion and Clinker Properties in Rotary Cement Kilns, Fuel. 2021. Vol. 283. P. 118951. DOI: 10.1016,j.fuel.2020. 118951.

13. A. Fakt, Evaluating Heat Transfer Conditions in a Plasma-Heated Rotary Kiln for Cement Production, Industrial & Engineering Chemistry Research. 2025. Vol. 64, no. 16. P. 8329–8338. DOI: 10.1021, acs.iecr.5c00220.

14. Moumin G., Tescari S., Sattler C. Impact of Bed Motion on the Wall-to-Bed Heat Transfer for Powders in a Rotary Kiln and Effect of Built-Ins , International Journal of Heat and Mass Transfer. 2021. Vol. 177. P. 121473. DOI: 10.1016,j.ijheatmasstransfer.2021.121473.

15. J. Seiden Becher , Temperature Analysis in Flighted Rotary Drums and the Influence of Operating Parameters, Chemical Engineering Science. 2021. Vol. 229. P. 115972. DOI: 10.1016,j.ces.2020.115972.

16. J. Seiden Becher, Experimental Analysis of the Flight Design Effect on the Temperature Distribution in Rotary Kilns, Chemical Engineering Science. 2021. Vol. 240. P. 116652. DOI : 10.1016,j.ces.2021. 116652.

17. B. Liu, Influence of Baffles on Mixing and Heat Transfer Characteristics in an Intern ally Heated Rotating Drum, Powder Technology. 2022. Vol. 398. P. 117129. DOI: 10.1016,j.powtec.2022.117129.

18. M. Adepu , Experimental Investigation of Conduction Heat Transfer in a Rotary Drum Using Infrared Thermography , Chemical Engineering Science. 2021. Vol. 230. P. 116145. DOI: 10.1016,j.ces.2020. 116145.

19. E. Ardalani , DEM Analysis of the Thermal Treatment of Granular Materials in a Rotary Drum Equipped with Baffles , Chemical Engineering Science. 2022. Vol. 251. P. 117476. DOI: 10.1016,j.ces.2022. 117476.

20. E. Ardalani , Heat Transfer of Cohesive Particles in a Rotary Drum: Effect of Material Properties and Processing Conditions , Powder Technology. 2024. Vol. 447. P. 120215. DOI: 10.1016 ,j. pewtec. 2024.120215.

21. Q. Jian, Numerical Study of Particle Behaviours and Heat Transfer in a Complex Rotary Kiln, Particuology. 2024. Vol. 92. P. 81–94. DOI: 10.1016,j.partic.2024.04.004.

22. E. Ardalani , Scale-Up of Heat Transfer in a Rotary Drum Equipped with Baffles, Powder Technology. 2023. Vol. 429. P. 118879. DOI: 10.1016,j.powtec.2023.118879.

23. F. Qi , Revealing Baffle-Enhanced Heat Transfer Mechanism in an Indirectly Heated Rotary Kiln by Discrete Element Method Modeling, Applied Thermal Engineering. 2025. Vol. 266. P. 125452. DOI: 10.1016, j. applthermaleng.2025.125452.

24. X. Zhu , DEM Simulation of a Rotary Drum with Inclined Flights Using the Response Surface Methodology , Processes. 2023. Vol. 11, no. 5. P. 1363. DOI: 10.3390,pr11051363.

25. Jacob R. M., Tokheim L.-A. Novel Design of a Rotary Calciner Internally Heated with Electrical Axial Heaters: Experiments and Modelling , Results in Engineering. 2023. Vol. 17. P. 100992. DOI: 10.1016,j.rineng. 2023.100992.

26. Maji A., Choubey G. Improvement of Heat Transfer Through Fins: A Brief Review of Recent Developments , Heat Transfer. 2020. Vol. 49, no. 3. P. 1658–1685. DOI: 10.1002,htj.21684.

27. Sadeghian Jahromi A., Wang C.-C. Heat Transfer Enhancement in Fin-and-Tube Heat Exchangers – A Review on Different Mechanisms , Renewable and Sustainable Energy Reviews. 2021. Vol. 137. P. 110470. DOI: 10.1016,j.rser.2020.110470.

28. Singh A. P., Ghoshdastidar P. S. Computer Simulation of Heat Transfer in Alumina and Cement Rotary Kilns , Journal of Thermal Science and Engineering Applications. 2022. Vol. 14, no. 3. P. 031001. DOI: 10.1115,1.4051376.

29. Mungyeko Bisulandu B.-J. R., Marias F. Modeling of the Thermochemical Conversion of Biomass in Cement Rotary Kiln , Waste and Biomass Val-orization. 2021. Vol. 12. P. 1005–1024. DOI: 10.1007,s12649-020-01001-9.

30. Mungyeko Bisulandu B.-J. R., Marias F. Numerical Modeling of Thermo-chemical Conversion of Biomass and Tires as Fuels for Cement Clinker Pro-duction , Recycling. 2023. Vol. 8, no. 2. P. 41. DOI: 10.3390, recycling8020041.

31. Cecílio D. M., Mateus M., Ferreiro A. I. Industrial Rotary Kiln Burner Performance with 3D CFD Modeling , Fuels. 2023. Vol. 4, no. 4. P. 454–468. DOI: 10.3390,fuels4040028.

32. Lahaye D., Juretić F., Talice M. Modelling a Turbulent Non-Premixed Combustion in a Full-Scale Rotary Cement Kiln Using Reacting Foam , Ener-Gies. 2022. Vol. 15, no. 24. P. 9618. DOI: 10.3390,en15249618.

33. H. F. Elattar , Swirled Jet Flame Simulation and Flow Visualization Inside Rotary Kil-n–CFD with PDF Approach , Processes. 2020. Vol. 8, no. 2. P. 159. DOI: 10.3390,pr8020159.

34. J. L. Ferrin , Modelling Oxy-Combustion Dynamics in Rotary Kilns for Sustainable Sili-con Production: A Case Study from the Sisal Project, Case Studies in Thermal Engineering. 2025. Vol. 70. P. 106058. DOI: 10.1016,j.csite.2025.106058.

35. E. Fedorova , Review: Axial Motion of Material in Rotary Kilns , Eng. 2025. Vol. 6, no. 6. P. 106. DOI: 10.3390,eng6060106.

36. Saruwatari M., Nakamura H. Coarse-Grained Discrete Element Method of Particle Behavior and Heat Transfer in a Rotary Kiln , Chemical Engineering Journal. 2022. Vol. 428. P. 130969. DOI: 10.1016,j.cej.

2021.130969.

37. Smoothed Particle Hydrodynamics Simulation of Transient Heat Transfer Within Rotary Kiln , L. Ding [et al.] , Advanced Powder Technology. 2024. Vol. 35, no. 7. P. 104543. DOI: 10.1016,j.apt.2024.104543.

38. H. Khodaei ,Eulerian CFD Simulation of Biomass Thermal Conversion in an Indirect Slow Pyrolysis Rotary Kiln Unit to Produce Biochar from Recycled Waste Wood , Energy. 2024. Vol. 288. P. 129895. DOI: 10.1016,j.energy.2023.129895.

39. Y. Wang, Novel Method for Temperature Prediction in Rotary Kiln Process Through Machine Learning and CFD, Powder Technology. 2024. Vol. 439. P. 119649. DOI: 10.1016,j.powtec.2024.119649.

40. Y. Xu, Two-Dimensional Temperature Field Prediction of Rotary Kiln Based on Graph Neural Networks, Physics of Fluids. 2025. Vol. 37, no. 2. P. 027145. DOI: 10.1063,5.0251395.

41. Attou Y., Bouhafs M., Feddal A. Numerical Analysis of Turbulent Flow and Heat Transfer Enhancement Using V-Shaped Grooves Mounted on the Rotary Kiln's Outer Walls , Journal of Thermal Engineering. 2024. Vol. 10, no. 2. P. 350–359. DOI: 10.18186,thermal.1448621.

42. J. Seiden Becher , Contact Heat Transfer Analysis in Flighted Rotary Drums, Thermal Science and Engineering Progress. 2024. Vol. 47.

P. 102265. DOI: 10.1016,j.tsep.2023.102265.

43. Chou S.-H., Hsiau S.-S., Liu S.-Y. Experimental Study of Heat Transfer and Transport Properties of Granular Material in Indirectly Heated Rotary Drums , International Journal of Heat and Mass Transfer. 2025. Vol. 238. P. 126485. DOI: 10.1016,j.ijheatmasstransfer.2024.126485.

44. He Y., E D., Jiang Z. Particle Motion and Gas–Solid Heat Exchange En-hancement in Rotary Drums with Aligned,Separated Flight , Processes. 2025. Vol. 13, no. 5. P. 1594. DOI: 10.3390,pr13051594.

45. C. Wang , Study on the Influence of Baffles on Heat Transfer Characteristics of Particles in an Oil Shale Rotary Kiln, Applied Thermal Engineering. 2025. Vol. 268. P. 125924. DOI: 10.1016,j.applthermaleng. 2025.125924.

46. H. Ma, A Review of Recent Development for the CFD–DEM Investigations of Non-Spherical Particles, Powder Technology. 2022. Vol. 412. P. 117972. DOI: 10.1016,j.powtec.2022.117972.

47. M. Wang , CFD–DEM Simulation of Heat Transfer and Reaction Characteristics of Pyrolysis Process of MSW Heated by High-Temperature Flue Gas, Processes. 2024. Vol. 12, no. 2. P. 390. DOI: 10.3390,pr12020390.

48. Wang J., Ku X., Yang S. Simulation of Biomass Pyrolysis in a Rotary Drum by Coupling CFD–DEM with a One-Dimensional Thermally Thick Model , Energy & Fuels. 2022. Vol. 36, no. 7. P. 3665–3679. DOI: 10.1021,acs.energyfuels.2c00050.

49. Bheda B., Tronstad J., Emady H. An Experimental Setup for Studying Conduction and Radiation Heat Transfer in a Rotary Drum , Chemical Engineering Science. 2025. Vol. 302. P. 120786. DOI: 10.1016,j. ces.2024.120786.

50. E. Ehlmé, An Assessment of Weighted-Sum-of-Grey-Gases Models for Computational Fluid Dynamics Modelling of Hydrogen Flames and Thermal Plasmas in Kilns, Applied Thermal Engineering. 2025. Vol. 278. P. 127401. DOI: 10.1016,j.applthermaleng.2025.127401